JOURNAL OF GEOPHYSICAL RESEARCH, VOL. 108, NO. B3, 2144, doi:10.1029/2001JB001738, 2003

Simulation of tensile crack generation by three-dimensional dynamic shear rupture propagation during an earthquake

L. A. Dalguer and K. Irikura
Disaster Prevention Research Institute, Kyoto University, Kyoto, Japan

J. D. Riera
Curso de Pós-Graduação de Engenharia Civil, Universidade Federal do Rio Grande do Sul,
Porto Alegre, Rio Grande do Sul, Brazil

Received 28 December 2001; revised 18 July 2002; accepted 18 November 2002; published 12 March 2003.

[1] As there is no evidence that cracks are created directly in modes II and III, shear cracks probably occur only along a weakness plane, as in a preexisting fault. Mode I fracture therefore may be an important factor in crack formation during shallow earthquakes. A three-dimensional shear dynamic rupture process was simulated on the assumption that shear slip occurs only in a preexisting fault and the possibility of introducing new internal cracks that propagate under tensile stress as a consequence of the dynamic process of shear slip propagation. The discrete element method (DEM) was used to solve this problem because it can introduce internal tensile cracks. The simple slip-weakening model was used as the friction law on the preexisting fault for shear rupture propagation. For new tensile cracks, fracture follows classical Griffith theory when the critical value for tensile fracture surface energy is reached. The proposed model was used to simulate the rupture process of a strike-slip shallow fault. Results show that the generation of new cracks is affected by rupture directivity in terms of the hypocenter and asperity location as well as by fault geometry with respect to the free surface. Cracks develop a flower-like structure that surrounds the preexisting fault. When the asperity is located at less than a certain depth, the flower-like structure that originates from the top of the fault reaches the free surface. We consider that this is the mechanism for forming the flower structure near surface during a strike-slip shallow earthquake. *INDEX TERMS:* 7209 Seismology: Earthquake dynamics and mechanics; 7260 Seismology: Theory and modeling; 8010 Structural Geology: Fractures and faults; *KEYWORDS:* rupture dynamic, shear and tensile cracks, fault mechanics, fault branching, earthquakes

Citation: Dalguer, L. A., K. Irikura, and J. D. Riera, Simulation of tensile crack generation by three-dimensional dynamic shear rupture propagation during an earthquake, *J. Geophys. Res.*, *108*(B3), 2144, doi:10.1029/2001JB001738, 2003.

1. Introduction

[2] Dynamic simulation of rupture processes during earthquakes usually is performed on the assumption that only shear slip (Mode II and/or III) occurs [e.g., *Andrews*, 1976; *Day*, 1982; *Olsen et al.*, 1997; *Fukuyama and Madariaga*, 1998; *Harris and Day*, 1999]. This is widely accepted in earthquake research because this phenomenon is considered a dynamically running shear crack [e.g., *Scholz*, 1990]. The rupture process of an earthquake, however, is known to involve superposition of the three basic modes (modes I, II and III) of dynamic fracture mechanics [e.g., *Atkinson*, 1987]. Certainly, modes II and III constitute the most important mechanism for generating seismic energy, ground motion, and shaking. For crack formation, because there is no evidence that natural faults appear directly under shear slip conditions, mode I may be a very important factor, especially in low-pressure zones like those in shallow earthquakes. In fact, laboratory findings indicate that a large number of tensile (mode I) microcracks are generated during shear slipping [e.g., *Cox and Scholz*, 1988; *Moore and Lockner*, 1995; *Anders and Wiltschko*, 1994; *Petit and Barquins*, 1988]. Numerical and field investigations of brittle faults by *Vermilye and Scholz* [1998] show that tensile microcrack zones occur within the volume of rock surrounding the fault tip. Such a zone may form before, during, or after growth of the shear plane. These findings for laboratory-induced shear fractures [e.g., *Cox and Scholz*, 1988], as well as for field investigations [e.g., *Vermilye and Scholz*, 1998], suggest that, unlike tensile fractures, low-pressure shear fractures do not grow by simple propagation within their own planes. Instead, they propagate by a complex breakdown process involving the interaction and coalescence of mode I microfractures. This idea comes from *Scholz* [1968] and *Lajtai* [1971], who concluded that shear cracks develop as a plane of shear failure only after a long history of tensile micro-

Copyright 2003 by the American Geophysical Union.
0148-0227/03/2001JB001738$09.00

fracturing. Interim steps include formation of individual tensile microcracks, the propagation and linkage of these cracks, and finally large-scale shear failure. Shear rupture is considered to propagate only along a weakness plane, such as a preexisting fault [*Scholz*, 1990].

[3] Considering the preceding laboratory and field findings, the numerical simulation of the dynamic rupture process in an earthquake involving the three basic modes (modes I, II and III) implies the assumption a preexisting fault for development of shear cracks and tensile stress concentrations resulting from slip on this fault cause mode I cracks that propagate away from the fault. A few numerical simulations that introduced tensile cracking during dynamic shear rupture have been reported. *Yamashita* [2000] used a 2-D finite difference formulation to investigate numerically the generation of tensile microcracks by dynamic shear rupture. In his model, microcracks always are separated by a fixed distance and are parallel locally. His simulation consists of a concentration of a swarm of cracks. These assumptions, however, do not allow for the linking between cracks to forms a new crack surface. *Vermilye and Scholz* [1998] and *Reches and Lockner* [1994] used quasi-static analyses to study the generation of microcracks but only inferred the orientation of microcracks from their analyses of quasi-static tensile stresses.

[4] We have used a 3-D numerical model to simulate the propagation of new tensile cracks as the consequence of spontaneous shear dynamic rupture along a preexisting fault. The discrete element method (DEM), which models any orthotropic elastic solid, was used. The modeled region is represented by means of a three dimensional periodic truss-like structure with cubic elements interconnected by unidimensional bars with lumped nodal masses (Figure 1). It was successfully used to simulate the dynamic shear rupture process of the 1999 Chi-chi (Taiwan) earthquake with a simplified 2-D model [*Dalguer et al.*, 2001a, 2001b]. For 3-D problems, *Dalguer et al.* [2002] calculated the dynamic shear stress changes during the rupture process of the 2000 Tottori earthquake, using the distribution of the fault slip and rupture time obtained from the inversion of strong motion waveforms. Detailed information on the DEM and its application to various 2-D dynamic problems related to the rupture process of an earthquake is described by *Dalguer* [2000]. The advantage of the DEM over the finite element method (FEM), boundary integral element method (BIEM), and finite difference method (FDM) is the ease of introducing internal tensile cracks with little computational effort and without increasing the number of degrees of freedom of the system.

[5] Our aim was to investigate numerically the formation of new cracks in the regions surrounding the source fault during an earthquake in a 3-D strike-slip shallow fault. The assumed preexisting fault, in which shear rupture propagation occurs, is embedded at a depth near the free surface. We show that new tensile cracks generated by the dynamic growth of shear rupture develop a flower-like structure that surrounds the preexisting fault and that some cracks reach the free surface.

[6] For shear rupture propagation, a simple slip-weakening model was used as the friction law on the preexisting fault. For new tensile cracks, however, fracture follows the classical linear elastic fracture mechanics (LEFM) theory [*Griffith*, 1920] when the critical value of tensile fracture surface energy is reached.

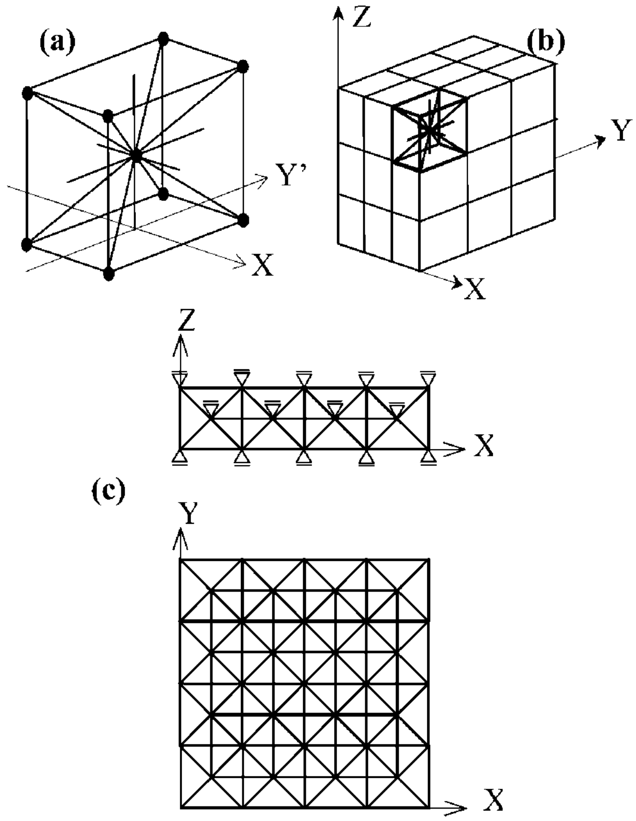

Figure 1. Numerical model used for the dynamic simulation (DEM). (a) Basic cubic module, (b) prismatic body generated for the 3-D model, and (c) representation of a plane strain state (no z displacements) for the 2-D model.

2. Formulation of the Discrete Element Method (DEM)

[7] The DEM was used to simulate 3-D dynamic shear rupture along a preexisting fault. In previous publications [e.g., *Dalguer et al.*, 2001a, 2001b] this model was used to solve only 2-D problems. An attractive feature of the proposed approach, however, is the possibility of accounting for the development of internal tensile cracks during shear slipping along the preexisting fault with little computation and without increasing the number of degrees of freedom of the system. It was successfully applied to a 2-D mode I dynamic crack propagation problem by *Riera and Rocha* [1991], who correctly predicted the propagation velocity of tensile cracks without shear slipping.

[8] In our DEM formulation, orthotropic solids are represented by a three dimensional periodic truss-like structure that has cubic elements (Figure 1). This model is based on developments in aeronautical engineering, in which, for purposes of structural analysis, it often is necessary to establish the equivalence between truss-like structural systems and a continuous medium. *Nayfeh and Hefsy* [1978] established the equivalence requirements between a cubic arrangement (Figure 1) and an orthotropic elastic medium. As Figure 1 shows, solids are represented by an array of

normal and diagonal bars linking lumped nodal masses. In an isotropic elastic material, the cross-sectional axial stiffnesses of the longitudinal and diagonal bars in the equivalent discrete model (Figure 1) are given by [e.g., *Dalguer et al.*, 2001b]

$$AE_n = \phi E \Delta x^2 \tag{1}$$

with bar length of Δx and

$$AE_d = 2\delta\phi E \frac{\Delta x^2}{\sqrt{3}} \tag{2}$$

with bar length of $\sqrt{3}$ ($\Delta x/2$), respectively, where for approximately isotropic solids; i.e., solids with equal stiffness in the three orthogonal directions, $\phi = (9 + 8\delta)/(18 + 24\delta)$, $\delta = 9\nu(4-8\nu)$, ν is the Poisson's ratio and E is the Young's module of the material.

[9] Uniaxial elastic forces, *Fe*, that act along the bars are computed by means of the cross-sectional axial stiffness given by equation (1) or (2)

$$Fe_j = AE_j\varepsilon_j, \tag{3}$$

where ε is the axial deformation of the bar j ($j = n$ or d, the normal or diagonal bars, respectively).

[10] Representation of the elastic forces in the form given by equation (3) is very convenient for simulating tensile cracks, as explained later. Dynamic analysis was performed by means of an explicit numerical integration in the time domain. At each step of integration the nodal equilibrium, represented by equation (4), is solved by the central finite differences scheme:

$$m\ddot{u}_i + c\dot{u}_i = f_i, \tag{4}$$

where m denotes the nodal mass, c the damping constant, $\dot{u}_i$ and $\ddot{u}_i$ are components of the velocity and acceleration vectors, respectively, and f_i is a component of the resultant forces at one nodal point that include elastic, external, and frictional forces in the direction i of motion. In the current model, only those nodal points that coincide with the preexisting fault, once it breaks, are under frictional force governed by any predefined friction law. The damping constant, c, was assumed to be proportional to the rigidity, k, of the bars of each cubic element; i.e., $c = d_f k$, where d_f was assumed to be 0.005. It is a critical damping ratio (ξ) approximately less or equal to 0.045.

3. Friction Law on the Fault With Dynamic Shear Crack Propagation

[11] As stated, shear rupture propagates only along a weakness zone and involves sliding with friction. In our model, this zone is defined as a preexisting fault, in which only shear slip, governed by a friction law, takes place. We adopted the simple slip-weakening friction model in the form given by *Andrews* [1976]. This friction law, first proposed by *Ida* [1972], is used extensively for the dynamic simulation of fault rupture processes [e.g., *Day*, 1982; *Olsen et al.*, 1997; *Fukuyama and Madariaga*, 1998; *Harris and Day*, 1999; *Dalguer et al.*, 2001a, 2001b]. In addition to providing a plausible model for shear dynamic rupture propagation, its use is supported by experimental laboratory findings for sliding friction on rock [e.g., *Ohnaka et al.*, 1987].

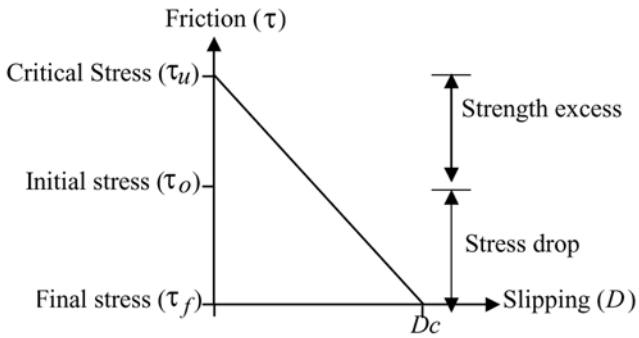

Figure 2. Slip-weakening friction model.

[12] The slip-weakening friction model is represented schematically in Figure 2. The shear force calculated from the resultant force, f_i, in equation (4) can be expressed by the shear stress, τ. The relationship between the shear stress, τ, and the slip of the fault, u, is expressed by

$$\begin{aligned} &\tau < \tau_u && u = 0 \\ &\tau = \begin{cases} -\dfrac{\tau_u - \tau_f}{D_c} u + \tau_u & 0 < u < D_c \\ \tau_f & u \geq D_c \end{cases} \end{aligned} \tag{5}$$

where τ_u is the critical stress or upper yield point, τ_f is the final stress or residual stress considered as the dynamic friction stress level, and D_c is the slip required for stress to drop to its dynamic friction level. We assume there is no back slip on the fault, therefore the slip velocity is always greater or equal to zero.

[13] On the basis of this formulation, the validity of the DEM to simulate shear dynamic rupture processes in 2-D has been demonstrated by *Dalguer et al.* [2001b] in connection with spontaneous in-plane rupture with the slip-weakening law analyzed by *Andrews* [1976]. The results are consistent with the solution presented by *Andrews* [1976]. The validity of the DEM approach for the 3-D problem is further discussed in Appendix A. Three problems previously analyzed by *Madariaga et al.* [1998] were solved: first, a circular shear fault that breaks instantaneously and does not propagate; second, spontaneous growth of rupture initiated from a circular asperity, which does not stop; and third, spontaneous growth of rupture on a finite circular fault. All the features of these dynamic rupture problems reported by *Madariaga et al.* [1998] are closely reproduced by the DEM. The dynamic rupture problems analyzed to verify the adequacy of the DEM for the 2-D [*Dalguer et al.*, 2001b] and 3-D models (see Appendix A) are consistent with the solutions presented in the specialized literature. The 2-D and 3-D DEM models are thus shown to be effective for studying spontaneous rupture propagation in a fault embedded in an elastic medium.

4. Constitutive Relationship for the Tensile Crack Propagation

[14] The behavior of uniaxial tensile stress-strain in rock [e.g., *Atkinson*, 1987] shows strain softening after peak

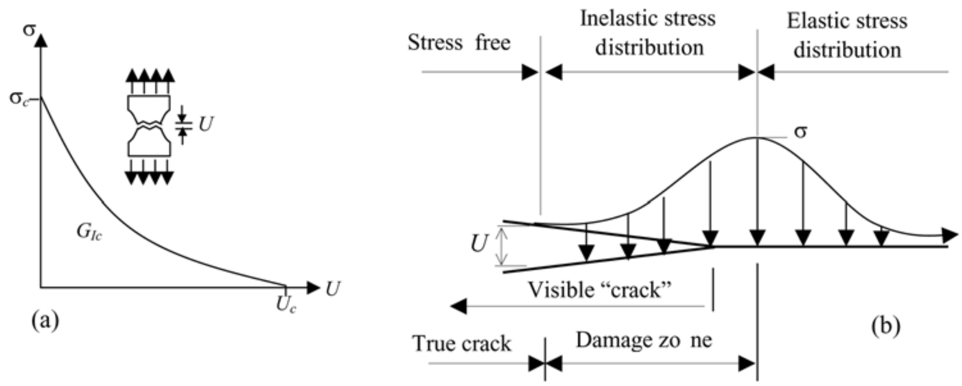

Figure 3. (a) Stress versus crack-opening displacement relationship obtained from a displacement-controlled, direct tension test [*Atkinson*, 1987]. (b) Schematic view of the hypothesized process zone [*Atkinson*, 1987].

stress has been reached. Therefore the constitutive model for pure mode I is stress versus crack-opening displacement (Figure 3a), obtained from the displacement-controlled direct tension test [*Atkinson*, 1987]. A material behaving in this manner would show gradual damage zone development (shown schematically in Figure 3b). This is related to the critical tensile fracture energy, G_{Ic}, of linear elastic fracture mechanics (LEFM), which has its roots in Griffith's energy balance concept. Therefore extension of a fracture occurs once G_{Ic} has been reached or exceeded. From Figure 3a, the critical fracture energy, G_{Ic}, is

$$G_{Ic} = \int_0^{U_c} \sigma(U)dU. \quad (6)$$

Use of DEM models, representations of elastic solids using discrete masses interconnected by unidimensional elements, is very convenient for simulating tensile cracking with the features shown in Figure 3. The constitutive relationship for the tensile stress-strain adopted for each bar element of the DEM is shown in Figure 4a. The loading-unloading path of the stress on each bar is shown in Figure 4b. A similar model was used successfully by *Riera and Rocha* [1991] to solve dynamic tensile crack propagation in 2-D problems. Because the stress and strain are in one-dimensional formulation, the critical tensile stress, σ_c, was derived from equation (3) or directly from Figure 4a as

$$\sigma_c = E\varepsilon_p, \quad (7)$$

where ε_p is the maximum elastic strain.

[15] From equation (6) and Figure 3, the critical fracture energy, G_{Ic}, for the DEM is the area of the inelastic zone of the stress-strain relationship shown in Figure 4a. Equation (7) gives

$$G_{Ic} = \frac{1}{2}E\varepsilon_p^2\Delta x(k_r - 1), \quad (8)$$

where Δx is the length of the element bar (grid size of the DEM.) and $k_r = \varepsilon_r/\varepsilon_p$, shown in Figure 4a, is the coefficient that defines strain softening after the peak stress has been reached until the crack totally opens. The critical tensile stress, σ_c, is calculated by use of a modified form of the classical Griffith equation [*Griffith*, 1920]

$$\sigma_c \cong \sqrt{\frac{EG_{Ic}}{\pi c}}, \quad (9)$$

where $2c$ is the preexisting crack length. For a crack in a linear elastic solid, G_{Ic} is expressed in terms of the critical stress intensity factor, K_{Ic}, in mode I. On the basis of Griffith's energy balance concept, it follows that

$$G_{Ic} = \frac{K_{Ic}^2(1-\nu^2)}{E}. \quad (10)$$

From equations (9) and (10), the critical stress intensity factor, K_{Ic}, is

$$K_{Ic} = \chi\sigma_c\sqrt{L}. \quad (11)$$

In the problem under consideration, L is the length of the preexisting fault and χ a nondimensional factor that depends on the geometry and grid size of the DEM. Equations (7), (10), and (11) verify that

$$\varepsilon_p = \frac{1}{\chi}\sqrt{\frac{G_{Ic}}{(1-\nu^2)LE}}. \quad (12)$$

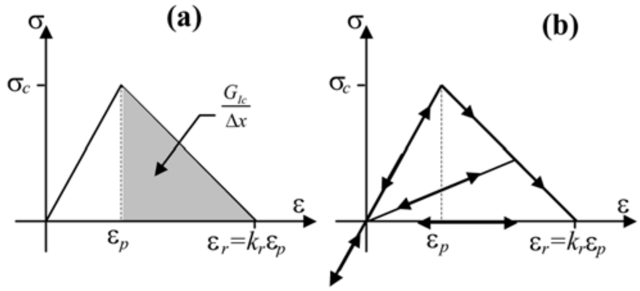

Figure 4. (a) Constitutive relationship for tensile crack generation used in the DEM. (b) The loading-unloading path of the stress on each bar.

The nondimensional factor, χ, is estimated by combining equations (8) and (12), giving

$$\chi = \sqrt{\frac{(k_r - 1)\Delta x}{2(1-\nu^2)L}} \qquad k_r > 1. \tag{13}$$

For the tensile crack propagation formulation given above, two parameters from a set of alternatives need to be previously defined; the critical tensile stress intensity factor, K_{Ic}, (or the critical tensile fracture energy, G_{Ic}), and the k_r coefficient.

[16] The proof of this formulation using the DEM is presented in Appendix B, for which purpose we solve the response of a rectangular plate in plane strain condition with an initial symmetrical crack [e.g., *Broek*, 1989]. This is a theoretical problem of Linear Elastic Fracture Mechanics (LEFM).

5. Generation of Tensile Cracks by Spontaneous Growth of Shear Rupture

[17] Numerical shear rupture simulation was obtained for near-field elastodynamic motion coupled to frictional sliding on a preexisting fault. Initially the stress distribution along the fault is at the initial stress level, and rupture starts artificially by imposing a stress drop in a limited small region, leading to stress accumulation along the fault that increase monotonically without relative slipping. Eventually, the interface shear stress (τ) at a point exceeds the local shear strength (critical stress level, τ_u) and slip at a node occurs, governed by the slip-weakening model represented by equation (5). Because seismic radiation and slip depend only on the stress change (stress drop) during the earthquake, not on the absolute stress, the initial stress (τ_0) over the entire fault is assumed to be zero. The parameters required to simulate the rupture process governed by the slip-weakening friction model therefore are the strength excess, stress drop, and critical slip.

[18] For the numerical tensile rupture simulation, tensile stress concentrations resulting from the shear slip on the preexisting fault were assumed to cause the cracks in mode I that propagate away from that fault. Extension of a fracture occurs once the critical tensile fracture energy, G_{Ic}, is reached or exceeded. Tensile fracture is governed by the constitutive relation for tensile stress-strain (Figure 4). Steps include the formation of individual microcracks, their propagation, and the linking of these cracks. In essence this is the mechanism for the generation of mode I cracks used in our formulation.

[19] The background stress distribution over the entire field is zero (uniform). Certainly this is not realistic, a triaxial tectonic stress field as a function of depth should be a better representation of the problem. The introduction of tectonic stress, however, implies uncertainty in the level of stress distribution in the field, presently unknown. Because we studied the formation of cracks near the free surface, where the prestress field becomes low, under this condition, we could assume that the dynamic stress created by shear rupture would be dominant over the background stress. The formation and possible patterns of the simulated cracks are due to the directivity of the dynamic stress created by the rupture process.

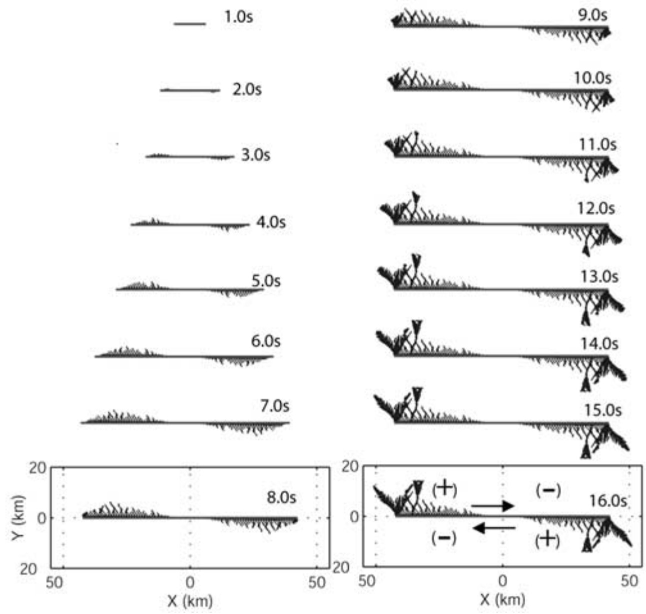

Figure 5. Snapshots (1 to 16 s) taken of shear rupture progress and the generation of tensile cracks. The horizontal solid line represents the shear crack, and irregular lines that leave the straight line represent tensile cracks.

5.1. Two-Dimensional Simulation

[20] Spontaneous in-plane rupture in the plane strain condition is simulated. The preexisting fault has the length L = 85 km. Fault movement is assumed to be right-lateral slip. Dynamic parameters for shear slipping, which are constant along the fault, are stress drop $\Delta\tau$ = 10 MPa, strength excess is 5.0 MPa, and critical slip D_c = 0.5 m. Rupture propagates bilaterally from the center of the fault with the stress drop constant everywhere along the shear crack plane. For generation of the tensile cracks, the critical fracture energy in mode I is assumed to be $G_{Ic} = 5 \times 10^5$ J/m^2 and the coefficient k_r = 1.5.

[21] A homogeneous medium is assumed with a P wave velocity of 6.1 km/s, S wave velocity of 3.5 km/s, and density of 2700 kg/m^3. It corresponds to a Young's modulus of 8.37×10^{10} N/m^2, a shear modulus of 3.35×10^{10} N/m^2 and a Poisson's ratio of 0.25. The numerical model consists of cubic cells with sides Δx = 0.5 km long. A time step of 0.05 s is used for the numerical integration of the equation of motion.

[22] Generation of the tensile cracks in the 2-D in-plane problem is shown in the snapshots every second for 16 s (Figure 5). The tensile cracks expand as shear rupture grows and propagate from the tip of the shear crack. A large number of cracks are generated, as expected, mainly on the dilatation side. The dilatation and compression sides are specified by the positive (plus) and negative (minus) signs, respectively, as shown in the last snapshot of Figure 5. Lengths of the new cracks increase gradually from the origin (hypocenter) to the end of the fault. At the end of

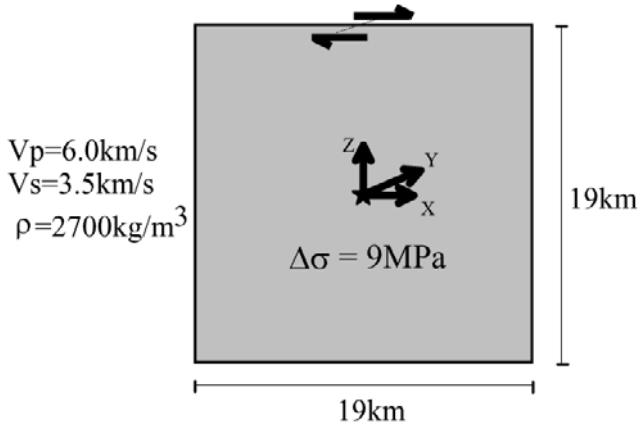

Figure 6. Homogeneous fault embedded in an unbounded medium with no free surface and the parameter distributions used in the 3-D dynamic simulation.

the preexisting fault the tensile cracks extend for long distances and form branches. The final stage of crack formation is consistent with that observed in the laboratory [e.g., *Petit and Barquins*, 1988], as well as with numerical analysis and field observations [e.g., *Vermilye and Scholz*, 1998].

5.2. Three-Dimensional Simulation

[23] The formation of new cracks and how they reach the free surface during an earthquake was investigated numerically in a 3-D model of a strike-slip shallow fault.

[24] To visualize the path of new cracks without interference by the free surface, the rupture process of a fault embedded in unbounded medium with no free surface first was simulated. The geometry of the fault model is shown in Figure 6. The hypocenter is located in the middle of the fault. Fault movement is assumed to be right-lateral slip. The dynamic parameters for shear slipping are constant along the fault (stress drop $\Delta\tau$ = 9 MPa, strength excess is 2.0 MPa and critical slip D_c = 0.2 m). The medium is characterized by a *P* wave velocity of 6.1 km/s, *S* wave velocity of 3.5 km/s, and density of 2700 kg/m^3. This is called the ‘‘homogeneous model.’’ The numerical model is constructed using cubic cells having 0.5 km long sides. A time step of 0.05 s was used in the numerical integration of the equation of motion.

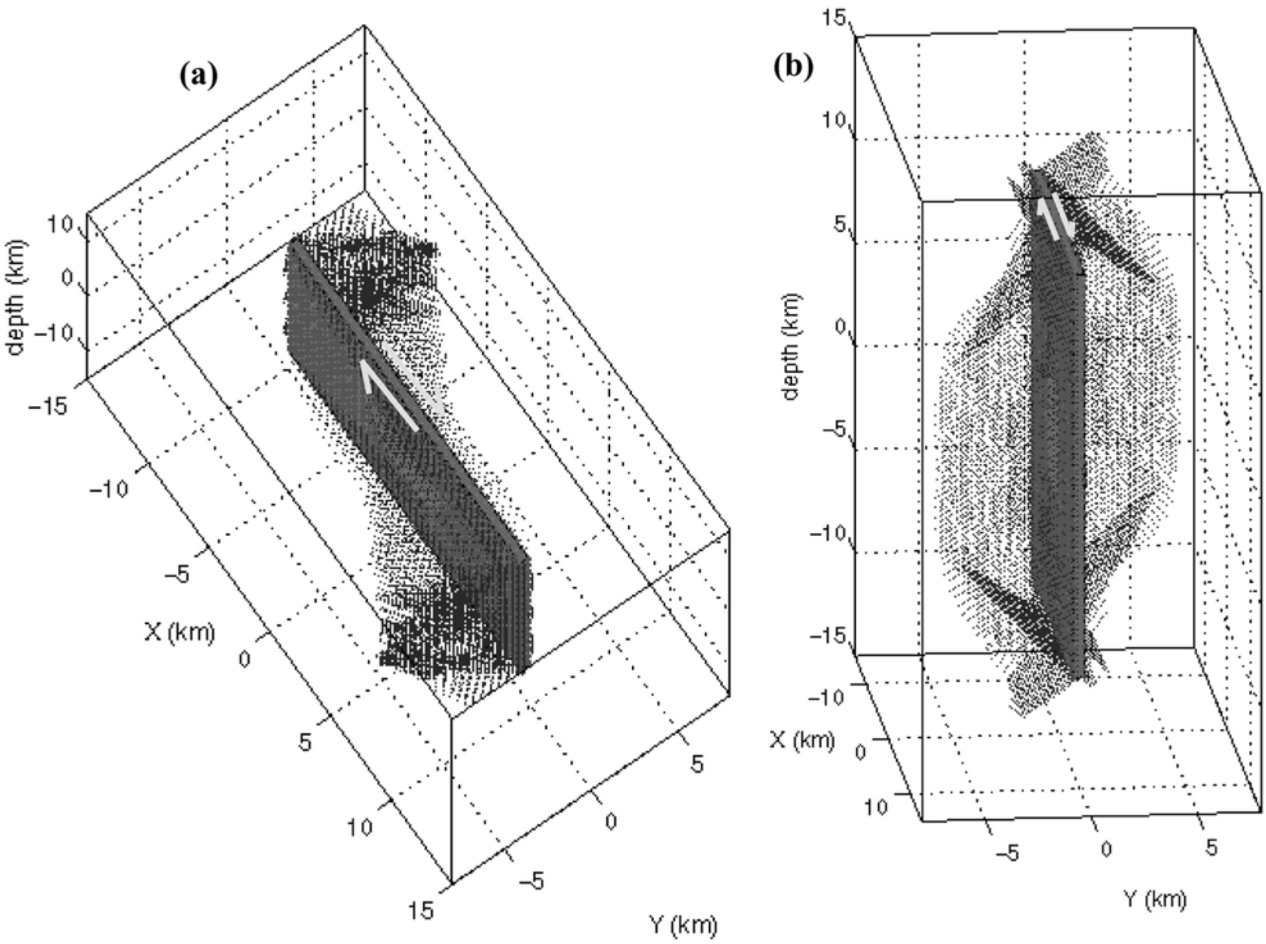

Figure 7. Two perspectives of the final stage of the crack evolution for a homogeneous fault model embedded in an unbounded medium with no free surface. Red denotes the shear crack on the preexisting fault, and blue denotes tensile cracks. (a) View of new surface cracks that grew from the sides of the fault and (b) view of new surface cracks forming flower-like structures that originated from the bottom and top boundaries of the fault. See color version of this figure at back of this issue.

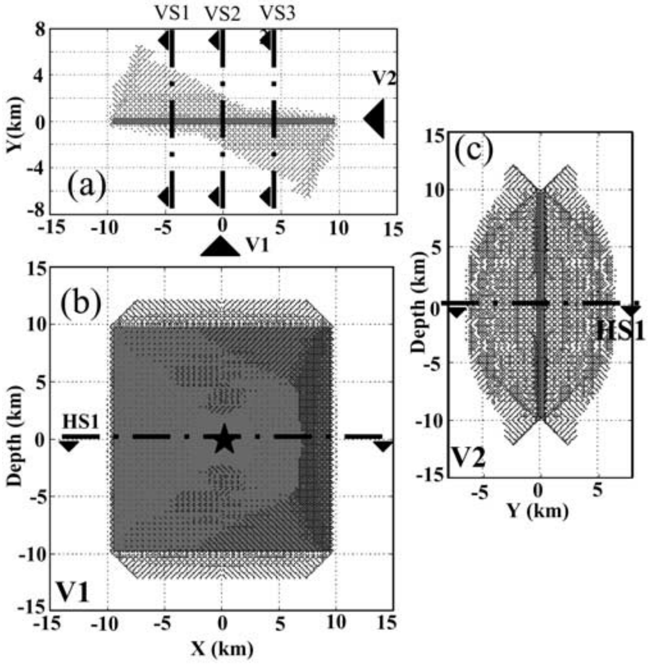

Figure 8. Views of the final stages of the crack evolution for a homogeneous fault model embedded in an unbounded medium with no free surface. (a) Bird's-eye view, (b) frontal view (V1), and (c) outline view (V2). See color version of this figure at back of this issue.

[25] For generating of the tensile cracks, a critical fracture energy in mode I, $G_{I\,c} = 5 \times 10^5$ J/m^2, and a coefficient k_r = 1.5 are assumed. These parameters were chosen to control the number of tensile cracks and to produce a clear crack formation pattern. For very low G_{Ic} values, the medium around the preexisting fault would be completely filled with cracks, making it difficult to distinguish the crack pattern. In contrast, at very high values no cracks would be generated. Some authors [e.g., *Atkinson*, 1987] suggest that G_{Ic} could be 1/10 to 1/100 smaller than the shear fracture energy. We tried to maintain this interval.

[26] Results for a homogeneous fault model embedded in an unbounded medium are given in Figures 7 to 9. Figure 7 shows two views of the final stage of the new cracks, in which new tensile cracks have grown, from the ends of the preexisting fault, forming very well defined new fractures with a flower-like structure. Figures 8a and 8c show a bird's-eye and an outline view of the fault, respectively, indicative that the orientation of the new cracks related to the two sides of the preexisting fault is asymmetric for the in-plane direction (mode II, Figure 8a) and symmetric for the antiplane (mode III, Figure 8c). Details of the characteristics of these cracks are seen in the vertical cross sections (VS1, VS2, and VS3) and the horizontal section (SH1) in Figure 9a. The location of these sections is given in Figure 8. In the horizontal section (SH1), which corresponds to the middle of the fault, the cracks have grown on the dilatational side of the in-plane direction. The vertical cross sections show that cracks are generated in the dilatation and compression sides of the fault, forming surfaces of cracks with a flower-like structure pattern. As shown in cross sections SV1 and SV3, three new surfaces are generated from the top and bottom of the fault; two grow from the two sides (dilatation and compression) of the fault toward its exterior domain and the other (only in the dilatation side) toward the interior domain of the fault. Crack length is longer in the dilatation than in the compression zone, the longest corresponding to cracks that grow toward the interior domain of the fault.

[27] On the basis of these results, tensile rupture patterns appear to grow only at angles of 45° and −45°. This suggests that maximum tensile stress occurs in this zone. Details of cracks generated in the numerical model are shown in Figure 9b. The geometrical form and grid size of each DEM element may constitute a limitation such that no cracks grow at any other angles.

[28] We next studied the free surface and the hypocenter location effects on the generation of tensile cracks. In the homogeneous model, the preexisting fault is embedded at a depth of 3 km from the free surface (Figure 10). Three cases, in which the hypocenter is located in the lower, middle, or upper part of the fault, were analyzed, called models M1, M2, and M3, respectively.

[29] Simulation results for these three cases (M1, M2, and M3) are given in Figures 11 to 14. Figure 11 presents two views of the final stage of the new cracks in all the cases. Figure 11a shows that in all of them the new crack surfaces that grew from the sides of the fault have similar characteristics, even in the fault model embedded in unbounded medium (Figure 7a). In contrast, Figure 11b shows that the new cracks were generated from the bottom and top boundaries of the fault, depending on the hypocenter's location. When compared with the fault model embedded in unbounded medium (Figure 7b), cracks originating from the top of the fault have a different pattern evolution, clearly showing the free surface effect on crack generation. These characteristics also can be seen in Figures 12a and 12c, which show a bird's-eye and an outline view of the fault, respectively. Details of the generation of cracks from the top and bottom of the fault are shown in the vertical cross sections VS1, VS2, and VS3 in Figure 13. The location of these sections is specified in Figure 12a. Figure 13 shows that the pattern of the new cracks (flower-like structures) that are formed from the top of the fault (near the free surface) differs from the pattern formed at the bottom. At the top of the fault, in the strike direction, two surfaces are generated symmetrically from the border of the two sides of the fault toward the free surface. At the bottom of the fault, new surfaces are generated as in the fault model with no free surface (Figure 9a). Evolution of cracks emanating from the bottom of the fault clearly is affected by the rupture directivity related to the hypocenter location, i.e., the farther the hypocenter from the border of the fault the longer the length of the crack. On the other hand, cracks that developed from the top of the fault are affected mainly by the free surface. In all the cases, the cracks reach the free surface. Apparently, the free surface causes an increase in the lengths of the cracks, as suggested when models M1 and M3 are compared. If there are no free-surface effects, the cracks on the top of the fault in model M3 should be equal to

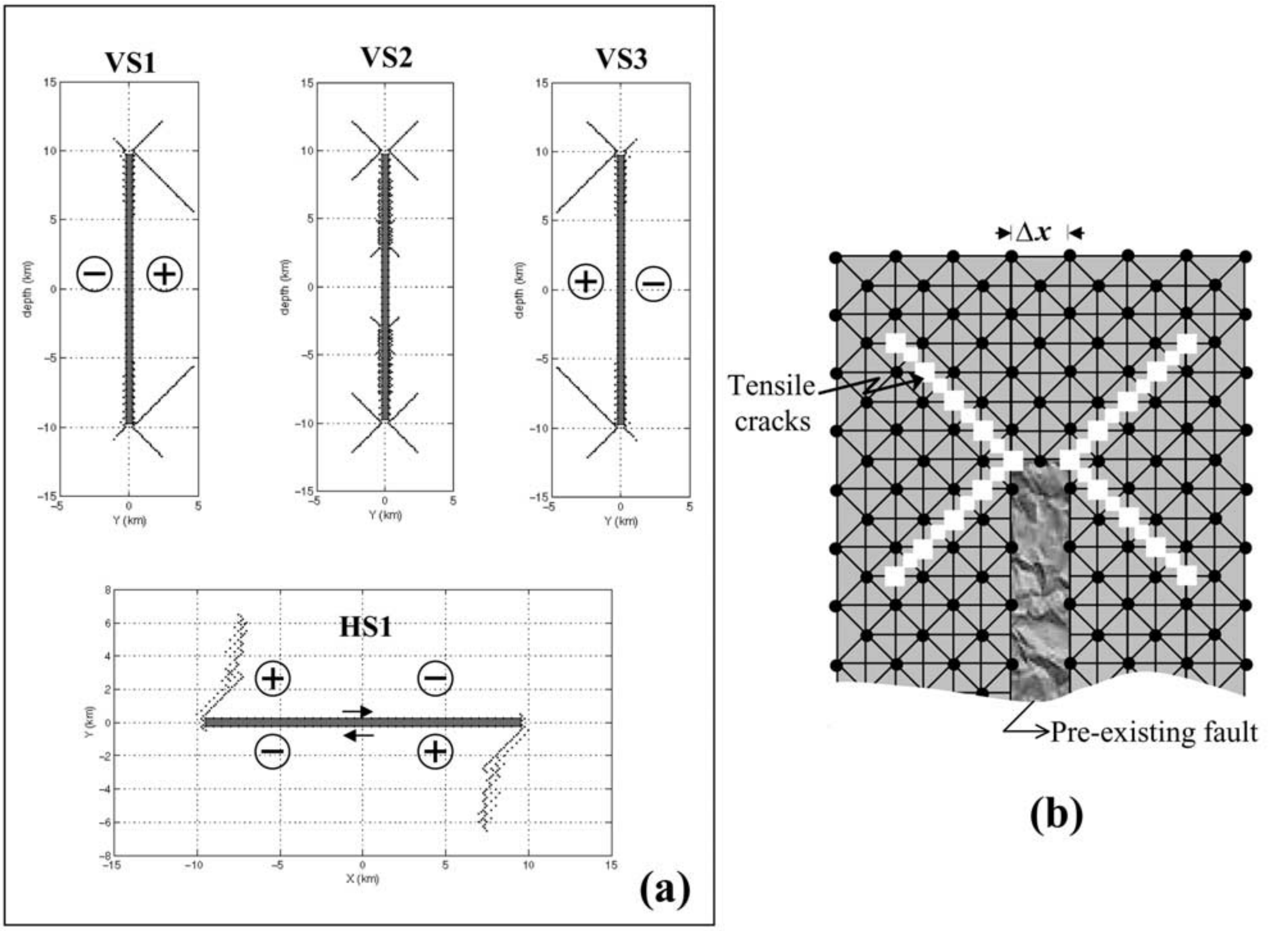

Figure 9. (a) Vertical, VS1, VS2, VS3, and horizontal, HS1, cross sections of the final stages of crack evolution in the homogeneous fault model embedded in an unbounded medium with no free surface. Section locations are given in Figure 8. The thick solid line represents the shear crack, and the irregular lines that leave it represent tensile cracks. Dilatation and compression sides are specified by positive (plus) and negative (minus) signs, respectively. (b) Schematic representation of the cracks generated in the numerical model, DEM, used for the dynamic simulation.

those in the bottom of the fault in model M1. Another effect of the free surface is that cracks that originated at the border of the fault and propagated toward the interior domain, as seen in the fault model with no free surface (Figure 9a), cease to develop.

[30] Horizontal section SH1 in Figure 14, which corresponds to the middle of the fault, as specified in Figures 12b and 12c, does not show any significant change between the cases. However, comparison of the surface rupture paths for model M3 with the path for models M1 and M2 shows marked differences. In models M1 and M2, cracks reach the free surface by forming a closed path around the trace of the fault; whereas in model M3 only two segments, which parallel the trace of the fault, are formed.

[31] A fault with an asperity embedded in a stratified medium (Figure 15) was used to analyze a more realistic earthquake source. An asperity was assumed to be a zone with a higher stress drop than the surrounding areas. The dynamic parameters for shear slipping are as follows: for

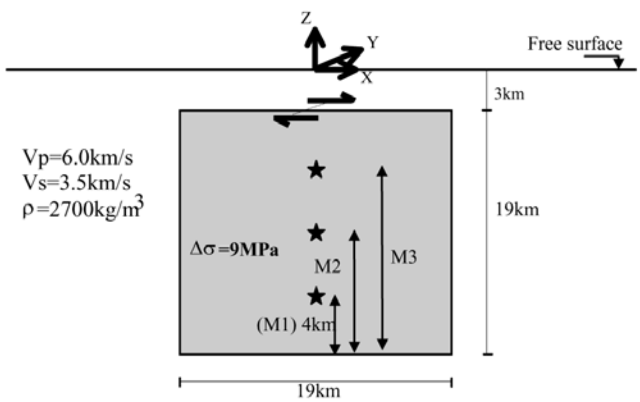

Figure 10. Homogeneous model for a preexisting fault embedded 3 km below the free surface and the parameter distributions used for the 3-D dynamic simulation. The stars represent hypocenter locations for the three cases, M1, M2, and M3.

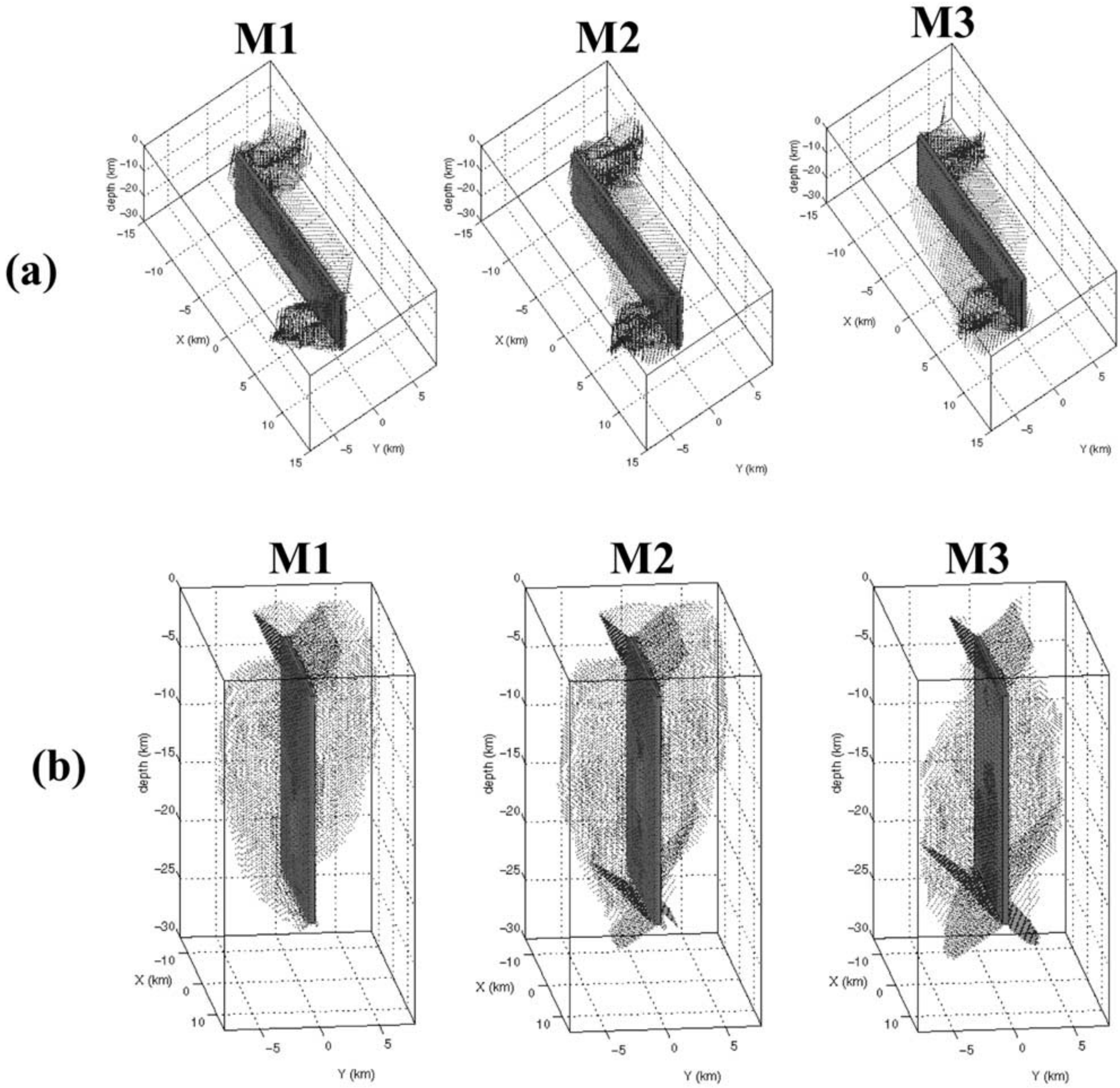

Figure 11. Perspectives of the final stage of the crack evolution for the homogeneous fault models (M1, M2, and M3) embedded 3 km below the free surface (a) View of new surface cracks that grew from the sides of the fault and (b) view of new surface cracks forming flower-like structures that originated from the bottom and top boundaries of the fault. See color version of this figure at back of this issue.

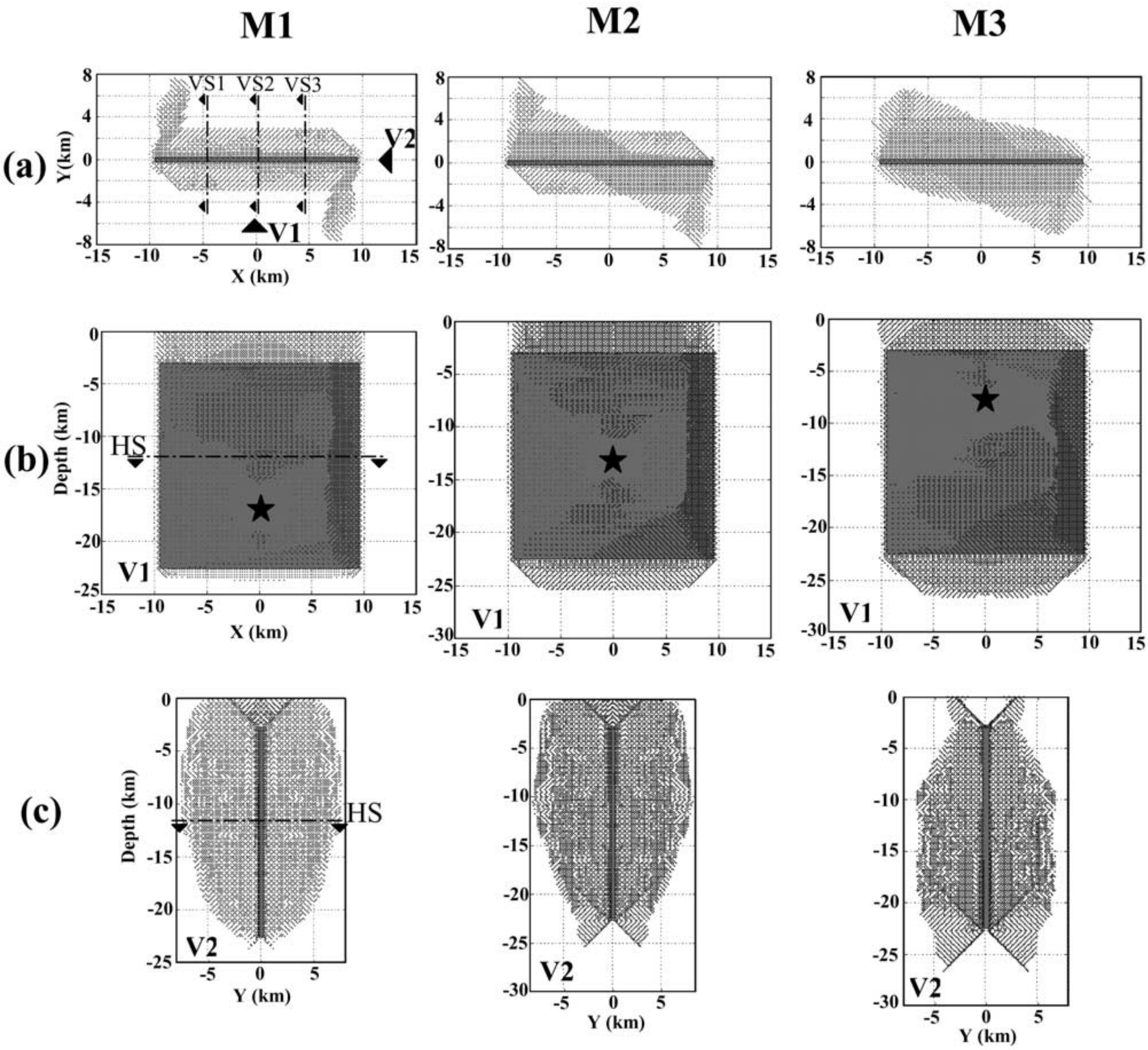

Figure 12. Views of the final stage of crack evolution for the homogeneous fault models (M1, M2, and M3) embedded 3 km below the free surface. (a) Bird's eye view, (b) frontal view (V1), and (c) outline view (V2). See color version of this figure at back of this issue.

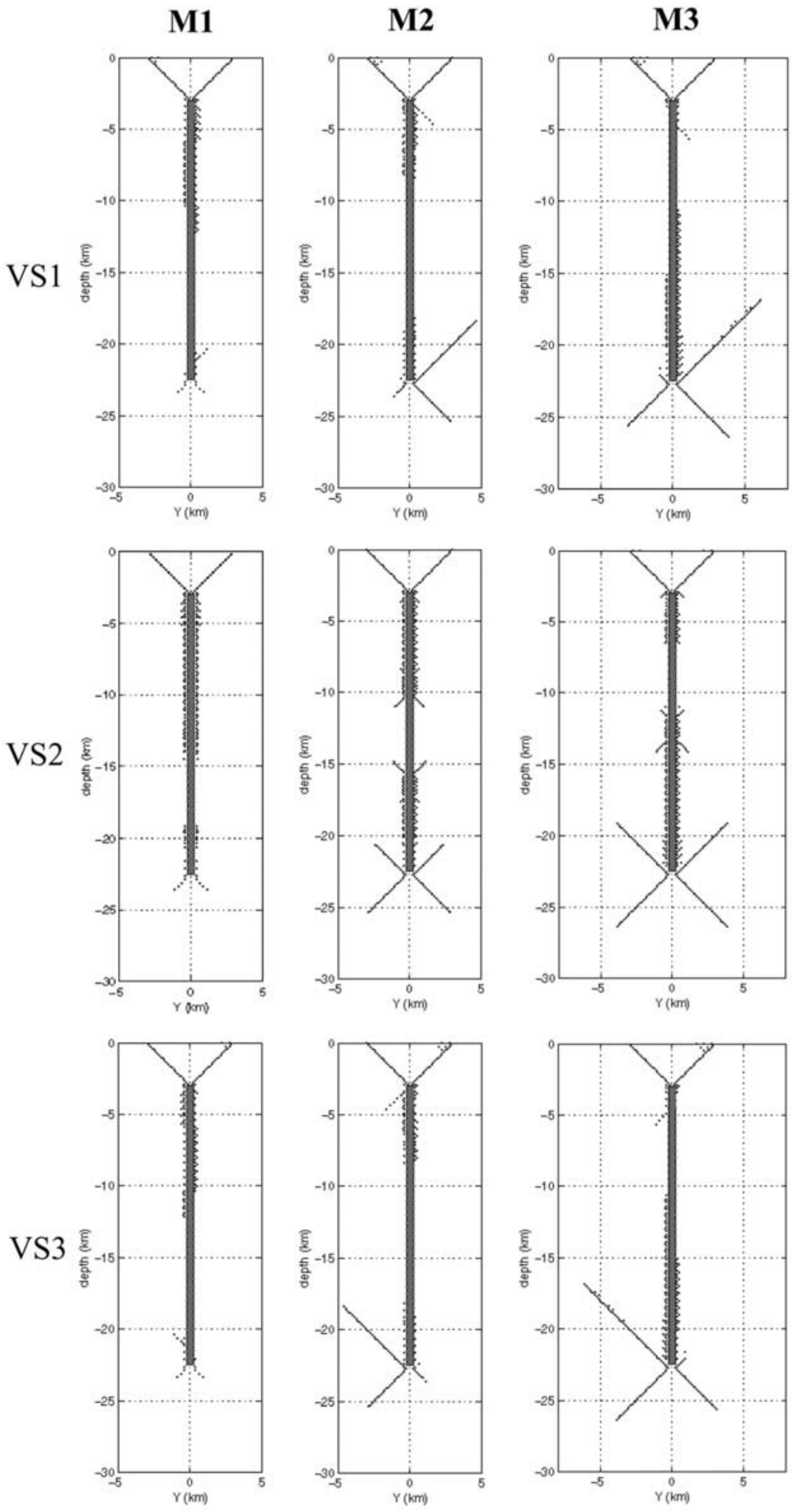

Figure 13. Vertical cross sections (VS1, VS2, and VS3) for the homogeneous fault models (M1, M2, and M3) embedded 3 km below the free surface. The location of these sections is specified in Figure 12a.

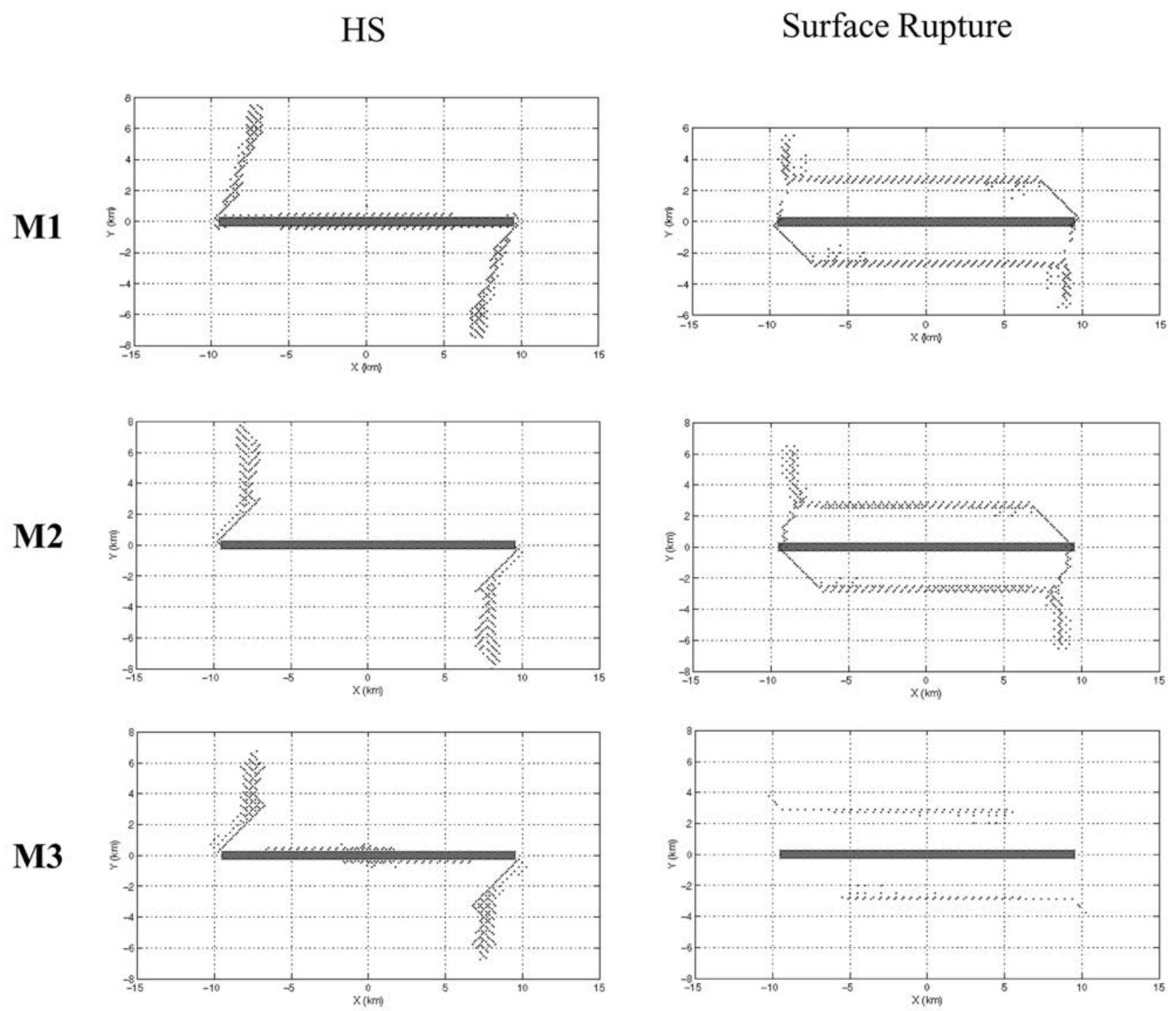

Figure 14. Horizontal cross section HS1 and surface rupture for the homogeneous fault models (M1, M2, and M3) embedded 3 km below the free surface. The sections HS1 are specified in Figure 12b.

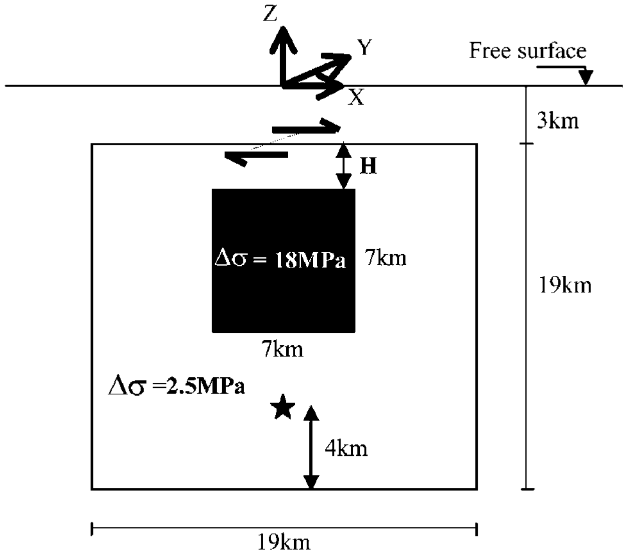

Figure 15. Asperity model with a preexisting fault embedded at a depth of 3 km from the free surface and parameters distribution used for the 3-D dynamic simulation.

the asperity area the stress drop $\Delta\tau$ = 18 MPa, strength excess of 3.0 MPa, and critical slip D_c = 0.5 m are assumed, and surrounding the asperity, the stress drop is $\Delta\tau$ = 2.5 MPa, strength excess of 3.0 MPa, and critical slip D_c = 0.15 m. For tensile crack generation, the same values as those in the homogeneous model are assumed. The velocity structure of the medium is shown in Table 1. This model is called the "asperity model". To study the effects of the asperity location on the propagation of new cracks, four cases with different asperity depths were simulated. In these models the values for distance H, from the top boundary of the fault to the top boundary of the asperity area, (see Figure 15) are H = 4.0, 3.0, 2.0, and 1.5 km.

[32] Simulations of new cracks corresponding to the asperity model for these four cases are shown in Figures 16 to 22. Bird's-eye, frontal, and side views of the preexisting fault are shown in Figures 16 to 19 for the models with H = 4.0, 3.0, 2.0, and 1.5 km, respectively. Figures 16–19 give a general view of the cracks. As seen previously in the homogeneous model, in the asperity models cracks also develop asymmetrically in the in-plane direction (mode II) and symmetrically in the antiplane (mode III). The frontal views (Figures 16b to 19b) show a concentration of cracks in the vicinity of the asperity zone. In general, all four cases have the same characteristics; cracks grow mainly from the borders of the asperity zone and from the top and lateral sides of the fault. No significant cracking occurs along the lower edge, unlike in the findings for the homogeneous model. This is due to the fact that the stress drop in the homogeneous model is greater than that in the area surrounding the asperity.

[33] Figure 20 shows vertical cross sections VS1, VS2, and VS3 for the four cases, for which locations are given in Figures 16a to 19a. The section along the middle of the asperity (VS2), in all the models, shows that cracks, which developed from the top of the fault and from the top and bottom of the asperity, were generated symmetrically on the two sides of the fault. In contrast, sections located outside the asperity (VS1 and VS3) show generation of asymmetric cracks. Those cross sections outside of the asperity show that the lowest cracks occurred at corresponding depths as at the bottom of the asperity, whereas the significant upper cracks originated only from the top of the fault. Cracks that developed from the bottom and top of the asperity have the same length in all the models, as seen in section VS2. In contrast, the lengths of cracks that originated from the top of the fault (sections VS1, VS2 and VS3) and from the bottom part outside the asperity (sections VS1 and VS3) increase as the asperity approaches the top of the fault. This increment in length is small for the bottom cracks, but is very large for the upper ones. The path of the asymmetric cracks originated from the top of the fault (see sections VS1 and VS2) is the same for the models in which H = 4.0, 3.0, and 2.0 km, but for H = 1.5 km the asymmetry is inverted, possibly because the cracks that originated from the top of the asperity in the model with H = 1.5 km extended to a depth of −2.5 km, exceeding the level of the top boundary of the fault, −3.0 km. Once cracks were generated from the top of the asperity extend beyond the top boundary of the fault, they and those generated from the top of the fault advance in parallel. This phenomenon may cause inversion of the increment of tensile stress on the two sides of the fault. Consequently, the asymmetry of the cracks that develop from the top of the fault also may be inverted, as in the model with H = 1.5 km and seen in sections VS1 and VS3.

[34] Our findings suggest that the effects of the asperity on the generation of cracks originating from the top of the fault increase as the asperity approaches the top. In the models with H = 4.0 and 3.0 km, these effects are slight; whereas in the models with H = 2.0 and 1.5 km they are marked.

[35] Figure 21 shows horizontal cross sections at the depths HS1, HS2 and at the free-surface rupture for the four cases. Sections HS1, located in the middle of the asperity (Figures 16b and 16c to 19b and 19c) in all the models, have similar characteristics; new cracks extend from the tip end of the fault and the tip end of the asperity on the dilatational side of the preexisting shear fault. Sections HS2, at 1.0 km below the free surface (shown in Figures 18b and 18c to 19b and 19c) show cracks that originated from the top of the fault in the models with H = 2.0 and 1.5 km, whereas these cracks in the other two models do not reach this level. The purpose of section HS2 is to show the difference in crack extension in the models with H = 2.0 and 1.5 km. The traces of these cracks, ∼2.5 km from the fault and parallel to the

Table 1. Velocity Structure for the Asperity Model

Depth, km	V_p, km/s	V_s, km/s	ρ, kg/m^3
0–2.5	4.5	2.6	2400
2.5–20	6.0	3.5	2700
20–∼	6.7	3.9	2800

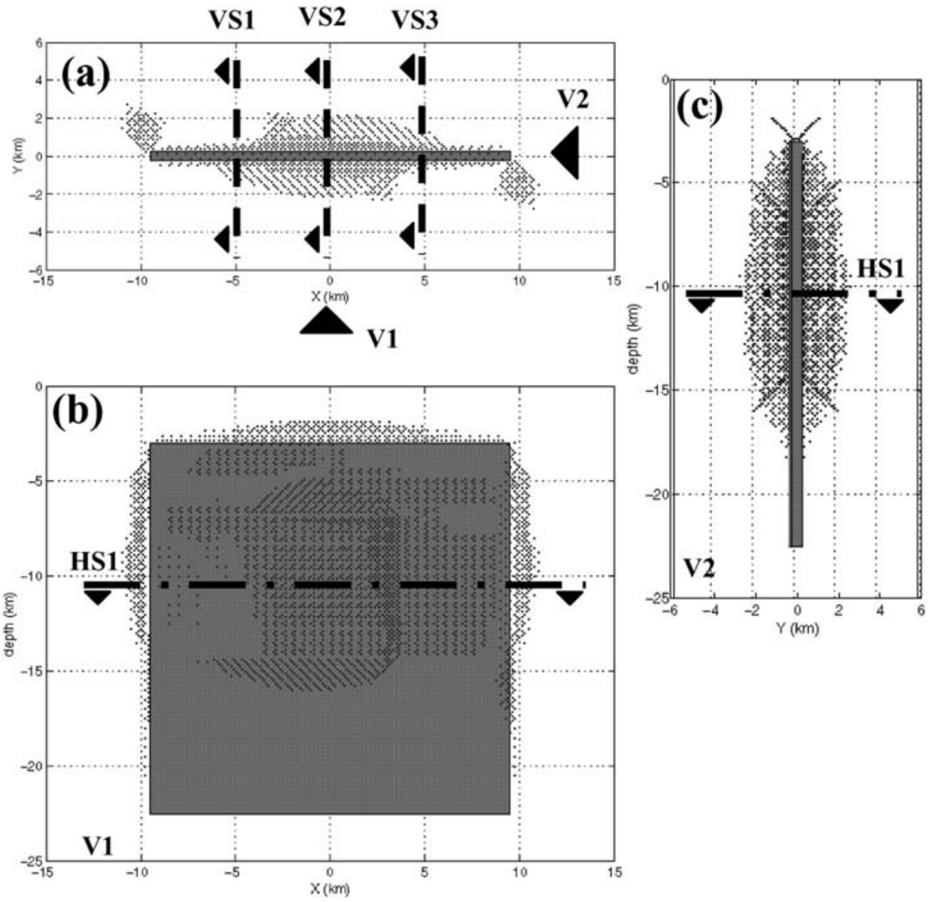

Figure 16. Views of the final stage of crack evolution for the asperity model (H = 4.0 km). (a) Bird's-eye view, (b) frontal view (V1), and (c) outline view (V2). See color version of this figure at back of this issue.

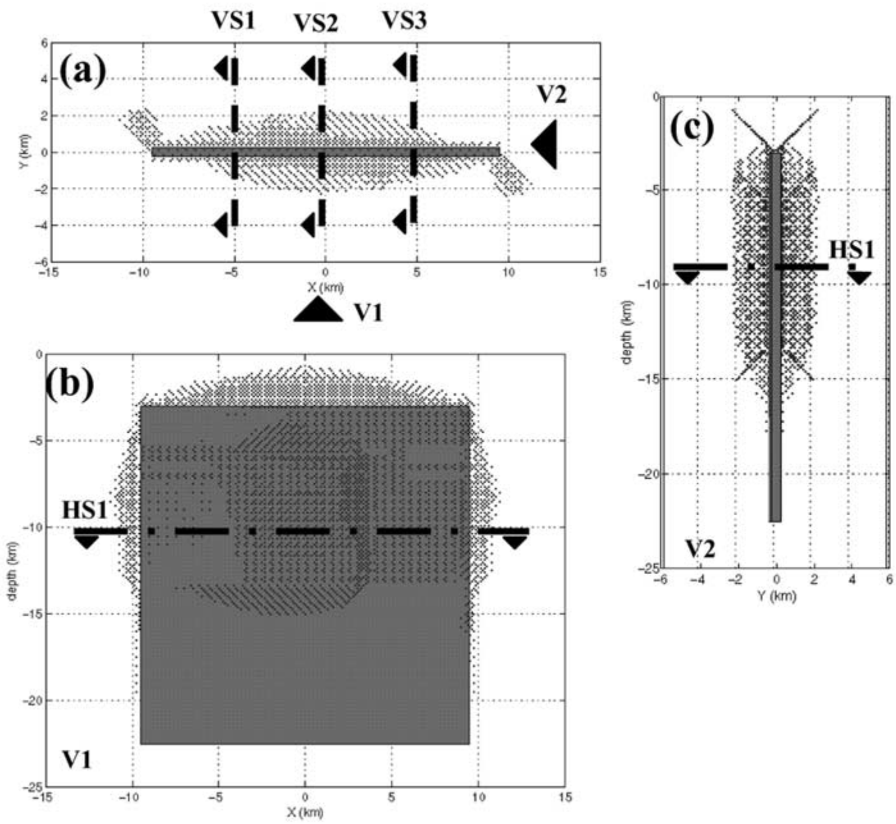

Figure 17. Views of the final stage of crack evolution for the asperity model (H = 3.0 km) (a) Bird's-eye view; (b) frontal view (V1); (c) outline view (V2). See color version of this figure at back of this issue.

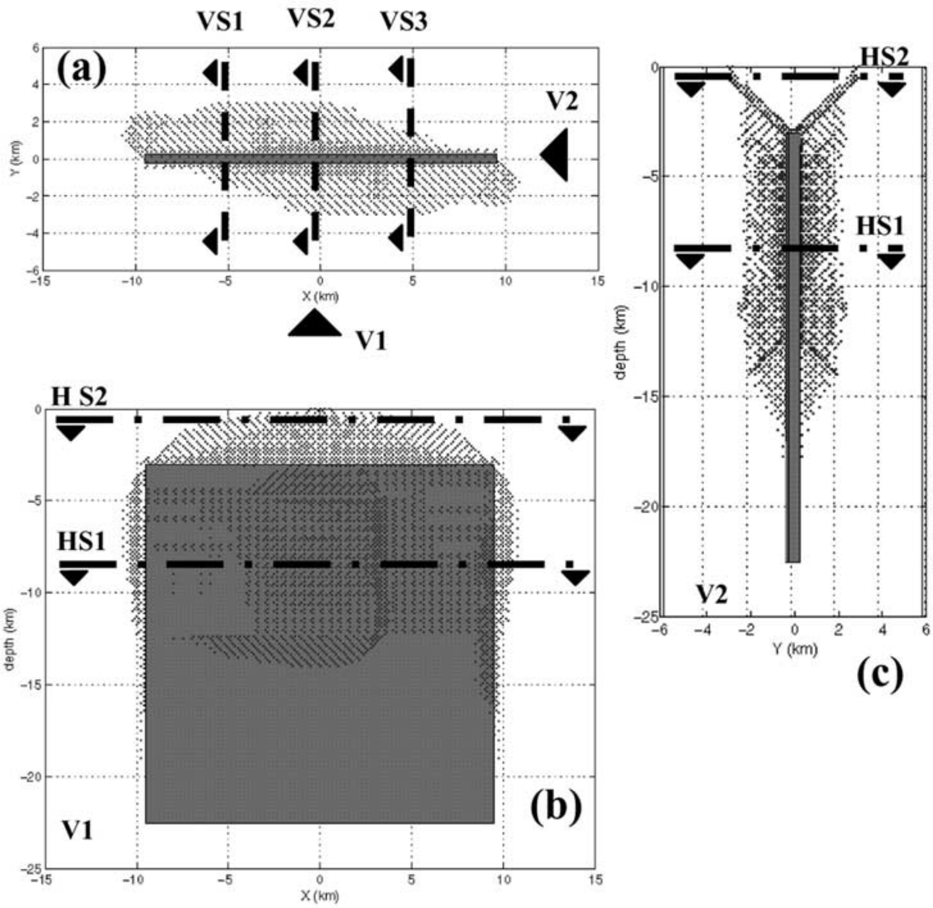

Figure 18. Views of the final stage of crack evolution for the asperity model (H = 2.0 km). (a) Bird's-eye view, (b) frontal view (V1), and (c) outline view (V2). See color version of this figure at back of this issue.

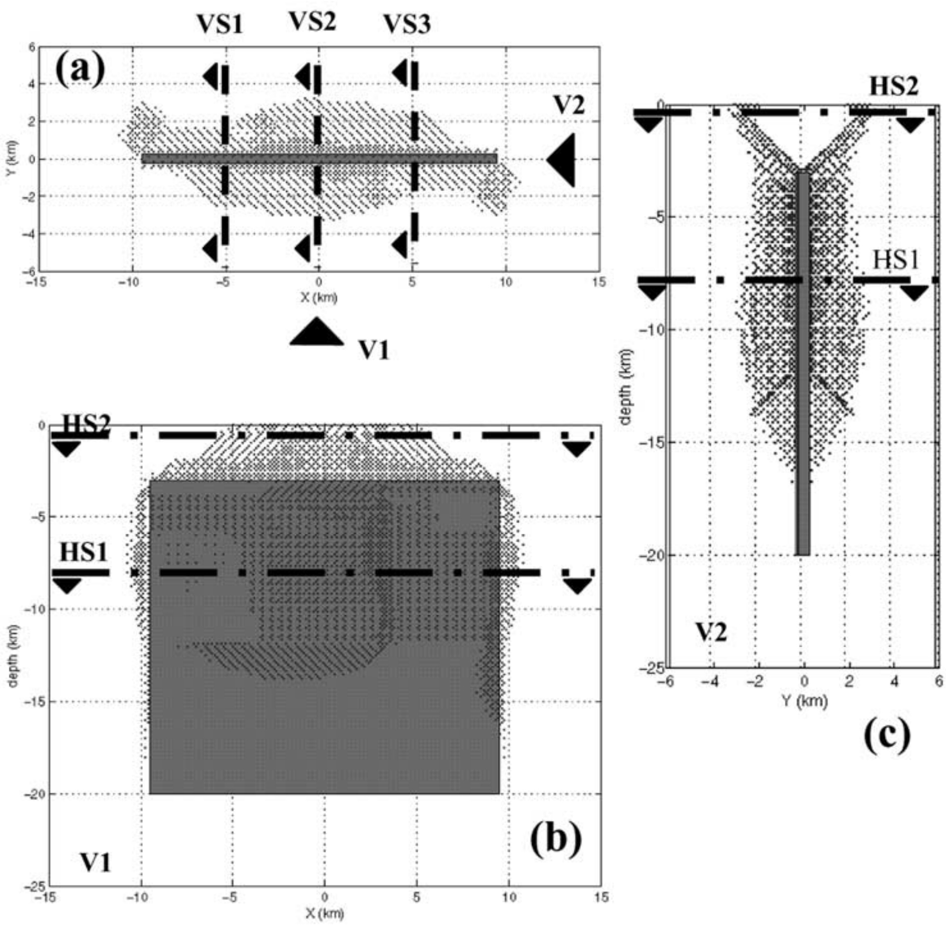

Figure 19. Views of the final stage of crack evolution for the asperity model (H = 1.5 km). (a) Bird's-eye view, (b) frontal view (V1), and (c) outline view (V2). See color version of this figure at back of this issue.

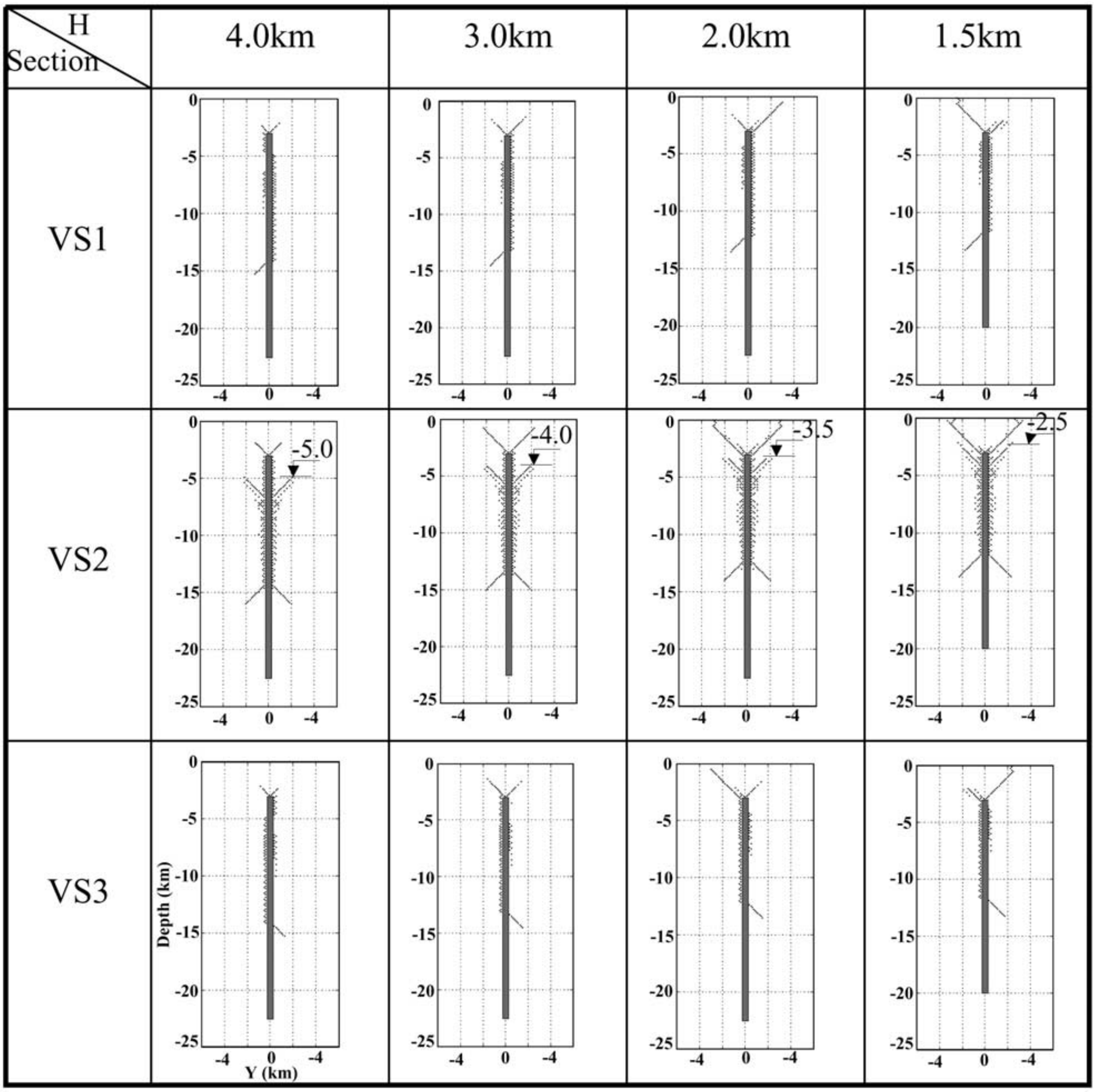

Figure 20. Vertical cross sections (VS1, VS2 and VS3) for the four cases of the asperity model. Section locations are given in Figures 16a to 19a.

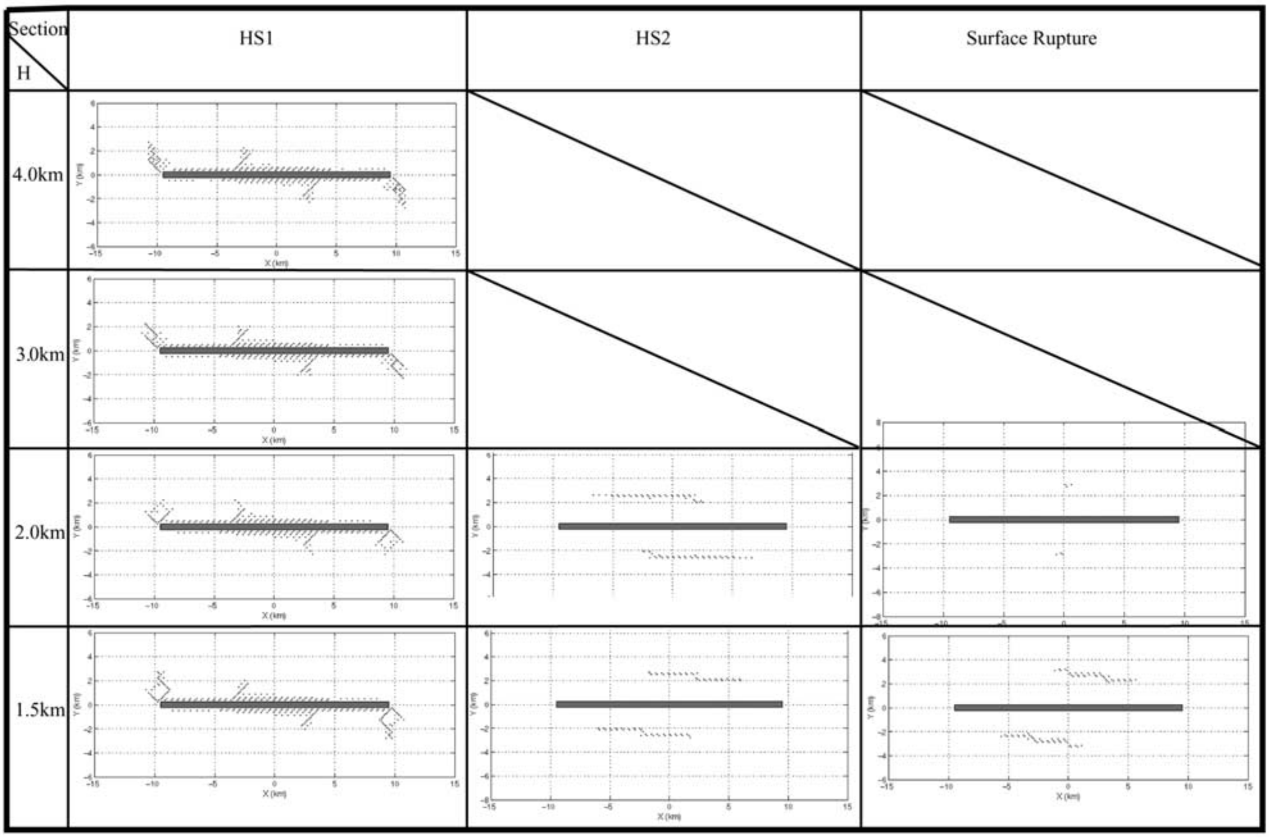

Figure 21. Horizontal cross sections (HS1 and HS2) and surface rupture for the four cases of the asperity model. HS1 sections are given in Figure 16b and 16c to 19b and 19c for each case. HS2 sections are specified in Figures 18b and 18c and 19b and 19c for H = 2.0 and 1.5 km, respectively.

preexisting fault, extend toward the dilatational side for the model with H = 2.0 km, whereas in the model with H = 1.5 km, crack extension is the opposite. As explained before, this may occurs because the increment in tensile stress at the top of the fault is inverted on the two sides. This inversion probably is caused by the proximity of the asperity to the top of the fault. Cracks that originate from the asperity reach the top of the fault then propagate parallel to the cracks that originated from the top of the fault.

[36] Surface rupture (Figure 21) occurs only in the models with H = 2.0 and 1.5 km. Cracks in the model with H = 2.0 km reach the free surface in a small zone ~3.0 km from the center of the trace of the preexisting fault. The model with H = 1.5 km, however, generates a surface rupture 6.5 km long on both sides of the fault. Under the assumptions given in the problem, the minimum condition for new cracks to reach the free surface seems to be that the asperity must be between 2.0 and 1.5 km below the top of the fault.

[37] Two perspectives of the final stage of the new cracks for the model with H = 1.5 km are shown in Figure 22 to provide a general view of these cracks. In Figure 22b the surfaces of the new cracks form a flower-like structure on top of the fault and on the bottom of the asperity. We consider it is the mechanism of the flower structure near surface during strike-slip shallow earthquake. On the lateral sides of the fault and asperity, however, cracks develop only on the dilatational side of the fault (Figure 22a).

6. Conclusions

[38] To our knowledge, this paper contains the first numerical 3-D simulation of the generation of tensile cracks by the dynamic shear rupture process along a preexisting fault during an earthquake.

[39] Because the rupture process of an earthquake involves a fracture dynamics problem, superposition of the three basic modes of rupture (modes I, II, and III) is required to describe the most general case of dynamic rupture propagation. The assumptions that new cracks are generated only by tension (mode I) and that shear sliding (modes II and III) occurs only along a preexisting fault are very well accounted for by the DEM.

[40] The 2-D simulation showed that tensile cracks expand as shear rupture progresses and propagate from the tip of the shear crack on the dilatational side of the fault. Moreover, new cracks at the end of the preexisting fault expand for long distances, and complex crack patterns are formed. This phenomenon was successfully simulated for the first time by numerical analysis (Figure 5).

[41] The 3-D simulation showed that cracks generated by shear slipping mainly propagate from the borders of the preexisting fault and asperity borders and form a flower-

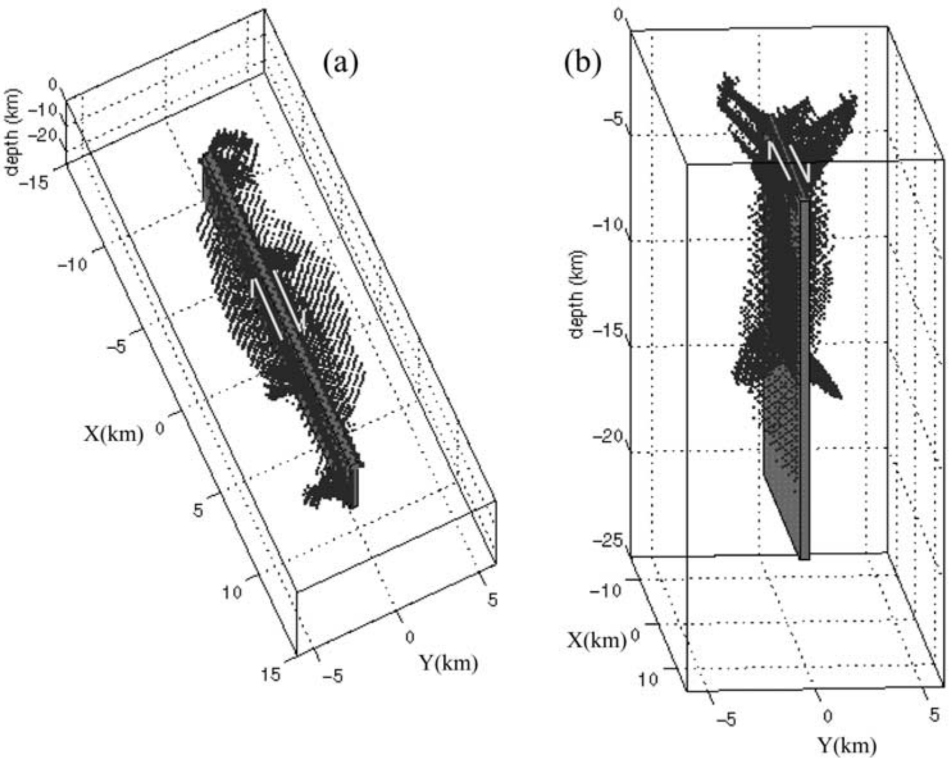

Figure 22. Two perspectives of the final stage of the crack evolution for an asperity fault model (H = 1.5 km). Red denotes the shear crack on the preexisting fault, and blue denotes tensile cracks. (a) View of new surface cracks that grew from the sides of the fault and (b) view of new surface cracks forming flower-like structures that originated from the bottom and top boundaries of the fault. See color version of this figure at back of this issue.

like structure. We consider this to be the mechanism that produces the flower structure near surface. The free surface and variations in hypocenter and asperity locations with depth markedly affect the cracks generated from the border of the fault and the free-surface rupture. The flower structures that originate from the top of the fault mainly are affected by the fault geometry with respect to the free surface, whereas those originating from the bottom mainly are affected by rupture directivity about the hypocenter location. This is interesting because even though the geological situation, such as the confining pressure dependent on depth, in which the pressure becomes low and the ground may be easy to break closer to the surface, is not include in our simulation, the free-surface effect was significant for creating this flower structure. This suggests that in a real situation, the dynamic stress created by shear rupture near the free surface could predominate over background stress, as assumed in the model described here.

[42] Whether the simulation is consistent with real earthquake behavior is still a question. During field observations reported by *Fusejima et al.* [2000] after the 2000 Tottori (Japan) earthquake, several small cracks were found on the free surface parallel to the causative fault. The traces of those cracks are similar to the ones shown in Figure 21 that correspond to the asperity model for H = 1.5 km. The seismic profiling from a reflection survey done in the 2000 Tottori (Japan) earthquake area and analyzed by *Inoue et al.* [2001] suggests that the flower structure developed near the free surface.

[43] Numerical analysis of the full dynamic rupture process of an earthquake based on the DEM provided truly encouraging results. The model and results we presented show that the DEM can be used successfully to predict fracture behavior during an earthquake and the formation of fault zones.

Appendix A: Validity of the DEM for Simulating a Shear Dynamic Rupture Process

[44] To verify the adequacy of the DEM to simulate a dynamic rupture process in 3-D, three problems presented by *Madariaga et al.* [1998] were analyzed: a circular shear fault that breaks instantaneously and does not propagate; spontaneous growth of rupture initiated from a circular asperity that does not stop; and spontaneous growth of rupture on a finite circular fault. The slip-weakening model was adopted as a friction law of the fault (equation (5) and Figure 2).

A1. Circular Shear Fault That Breaks Instantaneously and Does Not Propagate

[45] This problem was approximated by *Brune* [1970] and solved numerically assuming circular symmetry by

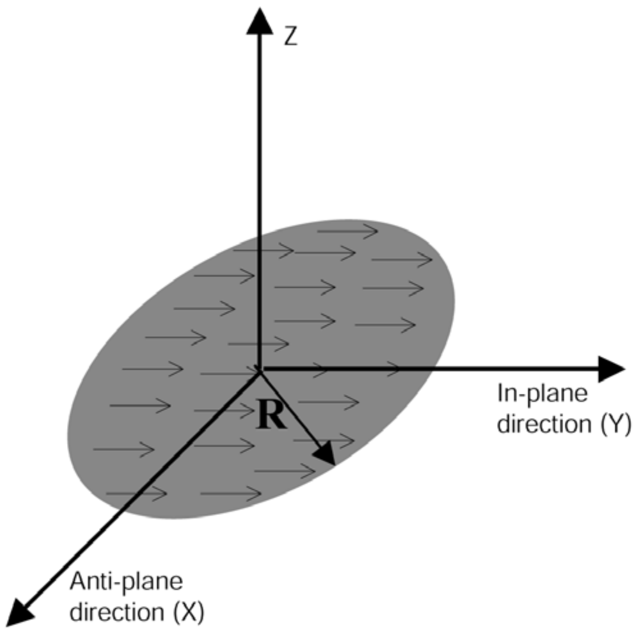

Figure A1. Theoretical circular fault with the radius R. The fault is on the x-y plane. Arrows show the direction of the slip.

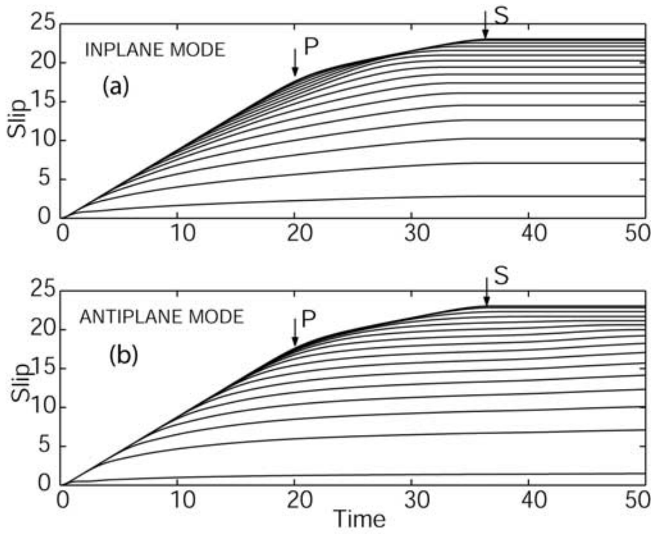

Figure A2. Slip as a function of time for instantaneous circular fault rupture solved by the DEM. Each curve represents the slip function at a different point along a radius of the fault. (a) Slip for the in-plane mode (along the y axis) and (b) slip for the antiplane mode (along the x axis).

Madariaga [1976]. *Madariaga et al.* [1998] also used this example to validate the finite diffenece method. In this problem, the fault is assumed to appear instantaneously in the medium and rupture to occur instantaneously inside a circular fault of radius R. The geometry of the problem is described in Figure A1, the circular fault is on the x-y coordinate plane, and slip is allowed only in the y direction; i.e., the x component of the slip is zero. The fault is embedded in a infinite homogeneous, isotropic elastic medium with a Poisson's ratio of 0.25, therefore $\alpha/\beta = \sqrt{3}$, where α is the P wave velocity and β the S wave velocity. The problem is solved for $\beta = 1$, $\alpha = \sqrt{3}$, density $\rho = 1$, rigidity $\mu = 1$, grid size $\Delta x = 1$, radius of the circular fault $R = 11\Delta x$. A simple Coulomb friction law is assumed along the fault, with a critical slip of $D_c = 0$. The critical stress is $\tau_u = 1$, and the initial stress $\tau_0 = \tau_u = 1$. This means that the strength excess is zero, therefore the fault is prestressed just before rupture, and the stress decreases instantly to zero at time $t = 0$. On the basis of these assumptions the stress drop, $\Delta\sigma$, is 1 everywhere in the rupture zone. Results are normalized by use of the scale of *Madariaga et al.* [1998] in Table A1.

Table A1. Results Normalized by Use of the Scale of *Madariaga et al.* [1998]

Parameter	Description
Distance along the fault	unit of Δx (grid interval)
Time	$t' = t\alpha/(H\Delta x)$ ($H = 1.0$)
Slip	$D' = D\mu/(2\Delta x\ \tau_u)$
Slip velocity	$\dot{D}' = \dot{D}\mu/(2\beta\tau_u)$
Stress:	$\tau' = \tau/\tau_u$

[46] Figures A2a and A2b show the slip function at different points along the radius of the fault for the in-plane direction (y axis) and antiplane mode (x axis), respectively. All the characteristics of the instantaneous rupture circular shear fault reported by *Madariaga et al.* [1998] are very well reproduced by the DEM. For example, they explain that after ~20 time units, the slip functions at the center of the fault show a break in slope corresponding to the arrival of the P stopping phase. After about 34 time units, the S stopping phase arrives, during which the fault stops slipping. Solutions for the in-plane and antiplane mode are similar but not exactly equal, therefore there is no cylindrical symmetry around the center of the fault.

A2. Spontaneous Growth of Rupture

[47] In this problem rupture initiates from a circular asperity, propagates spontaneously and does not stop. This example was solved by *Madariaga et al.* [1998] using the FDM model. The geometry of the problem is the same as that described in Figure A1. The radius of the circular fault that breaks instantaneously is $R = 10\Delta x$. The initial stress is $\tau_0 = 1.6\tau_u$ inside and $\tau_0 = 0.5\tau_u$ outside the asperity, and $\tau_u = 1.0$. In this problem the slip-weakening friction law is again used. In non-dimensional units the critical slip is $D_c = 4$, and the normalized units for all the variables are the same as in the previous example. $H = 0.35$ is used for the normalized time.

[48] Figure A3 shows results of the spontaneous growth of rupture. The slip and stress distributions on the fault, as functions of time and position along the in-plane direction, respectively are shown in Figures A3a and A3b. Figures A3c and A3d show the slip velocity

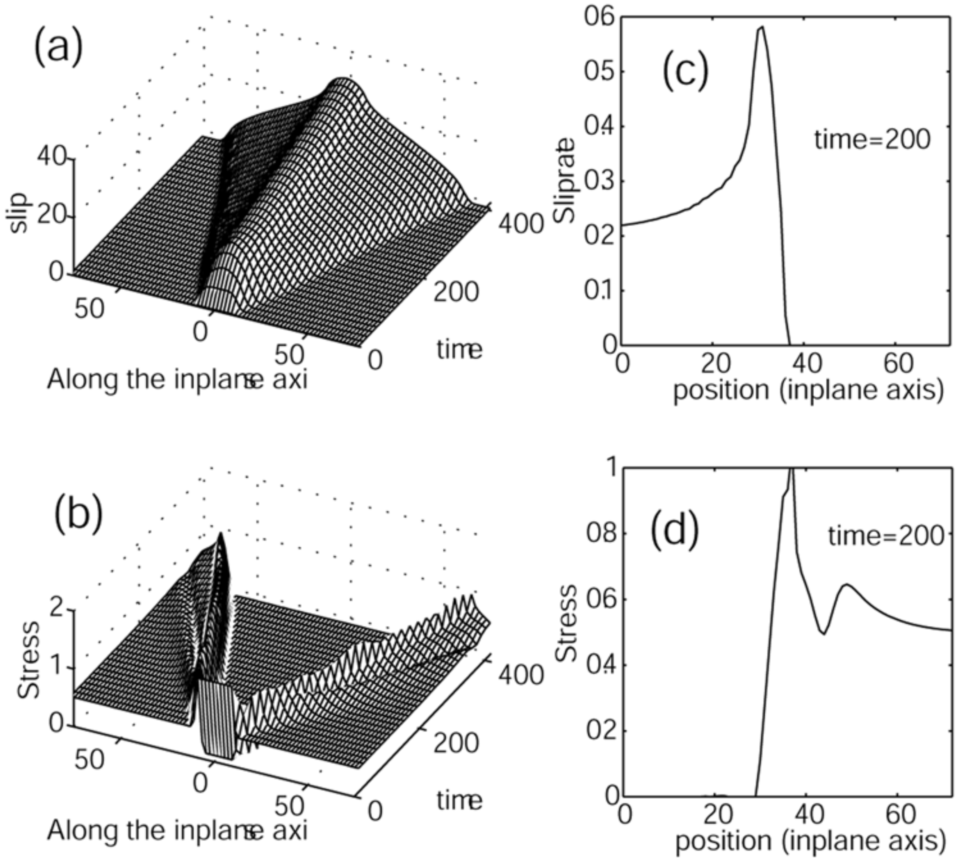

Figure A3. Numerical solution by the DEM of spontaneous growth of rupture, in which the rupture initiates from a circular asperity, propagates spontaneously and does not stop. (a) and (b) Slip and stress distributions, respectively, on the fault as functions of time and position along the in-plane direction. (c) and (d) Slip velocity and stress distribution, respectively, as the function of position along the in-plane direction at dimensionless time $t' = 200$.

and stress distributions, respectively, as functions of position along the in-plane direction at the dimensionless time $t' = 200$. Again, all the properties of the spontaneous growth of rupture reported by *Madariaga et al.* [1998] are closely reproduced by the DEM. For example, the peak of shear stress on the rupture front and the secondary peak associated with the S waves are very precisely described by the DEM (Figures A3b and A3d). This phenomenon originally was shown by *Andrews* [1976].

A3. Spontaneous Rupture on a Finite Fault

[49] In this problem rupture initiates from a concentric circular asperity and stops when it reaches the unbreakable boundary of a finite circular fault. This problem was solved by *Madariaga et al.* [1998] using the FDM model. The geometry coordinates of the problem are the same as in Figure A1. The circular fault has the radius $R = 50\Delta x$. Rupture starts from a concentric asperity with the radius $r = 6\Delta x$. The slip weakening friction law, with the critical slip $D_c = 4$, also is used. The initial stress is $\tau_0 = 1.2\tau_u$ inside the concentric asperity and $\tau_0 = 0.8\tau_u$ outside. Normalized units for all the variables are the same as in the previous examples. Simulation results are shown in snapshots of the slip velocity (Figure A4). DEM results also are very similar to those determined by *Madariaga et al.* [1998] with the FDM. Rupture grows faster in the in-plane direction which is dominated by mode II.

Appendix B: Validity of the DEM for Simulating Tensile Cracks

[50] To determine the adequacy of the DEM for simulating tensile cracks, we analyzed a theoretical problem of linear elastic fracture mechanics (LEFM). The response of a rectangular plate in the plane strain condition with an initial symmetrical crack [e.g., *Broek*, 1989] was solved. The relation of the applied stress, σ, and the stress intensity factor, K_I, for an arbitrary crack in an arbitrary body with arbitrary mode I loading is

$$\sigma = \frac{K_I}{\beta\sqrt{\pi c}}, \tag{B1}$$

where c is the size of the crack and β a geometrical factor (equivalent to χ of equations (11) and (13)). For any crack

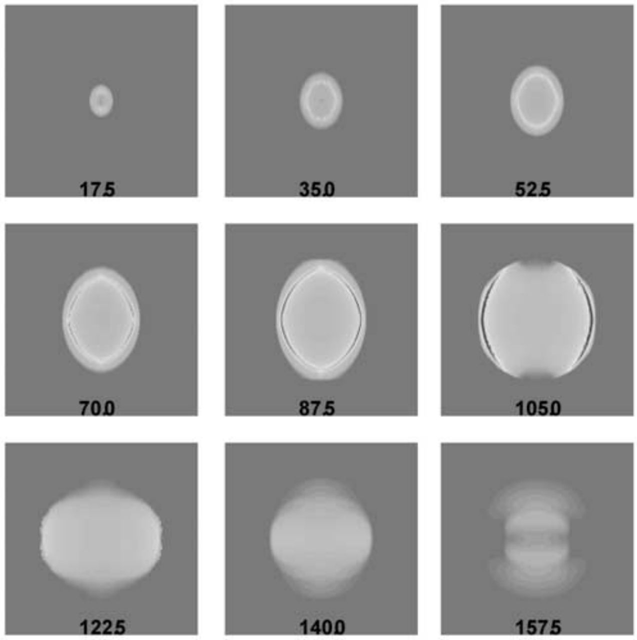

Figure A4. Snapshots of the slip velocity for a spontaneous rupture inside a finite circular fault determined by the DEM. Rupture starts with overloading of a concentric circular asperity inside the finite circular fault. The nondimensional time is shown at the bottom each picture.

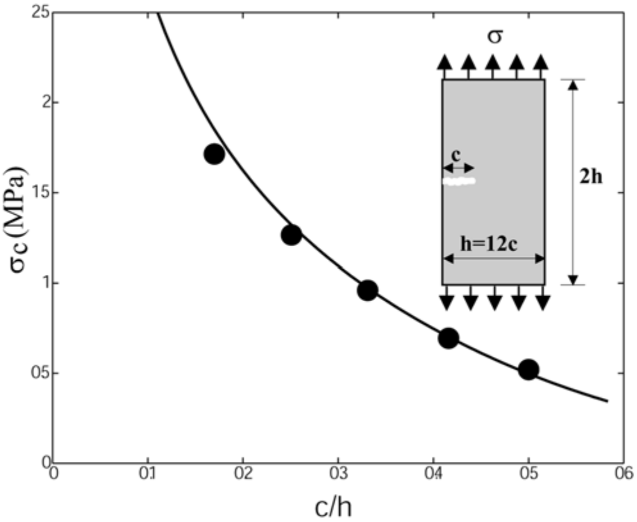

Figure B1. Critical stress response of a rectangular plate (0.12 m $\times$ 0.24 m) in plane strain condition with an edge crack solved by the DEM, also reported by *Riera and Rocha* [1991]. The solid curve represents the theoretical solution calculated by equation (B1). The dots represent five numerical tests for different crack sizes (c = 0.02, 0.03, 0.04, 0.05, and 0.06 m) solved by the DEM. The horizontal axis gives crack size normalized by the width of the plate.

in any practical problem only function β needs to be derived. The β functions for some common crack cases are given, for example, by *Broek* [1989].

[51] For our problem, a rectangular plate with an edge crack c, width h, and length $2h$ pulled to fracture with a tensile stress of σ as shown in Figure B1, function β is

$$\beta = 1.12 - 0.23\frac{c}{h} + 10.56\left(\frac{c}{h}\right)^2 - 21.74\left(\frac{c}{h}\right)^3 + 30.42\left(\frac{c}{h}\right)^4. \quad \text{(B2)}$$

For the given critical stress intensity factor, K_{Ic}, of any material, the theoretical critical stress σ_c applied on the plate can be calculated using equations (B1) and (B2).

[52] In this context, the DEM also can be used to predict numerically the critical stress and to compare the results with those obtained using equation (B1). This problem previously was solved with the DEM by *Riera and Rocha* [1991]; therefore their results are reproduced. These authors used a plate of width h = 0.12 m, length 0.24 m, and K_{Ic} = 0.611 MPa $\sqrt{m}$. The material property was assumed to have a Young's modulus of $E = 3.0 \times 10^{10}$ N/m^2, a Poisson's ratio of ν = 0.25, and specific mass of ρ = 2400 kg/m^3. The grid size of the DEM was Δx = 0.01 m. Five numerical tests for different crack sizes (c = 0.02, 0.03, 0.04, 0.05, and 0.06 m) were performed.

[53] Figure B1 shows the applied critical stress, σ_c, for the five tests calculated by the DEM. Values are compared with the theoretical solution calculated by equation (B1). Results are consistent with those for the theoretical prediction.

[54] **Acknowledgments.** This paper was supported by the Special Coordination Funds for Promoting Science and Technology titled "Study on the master model for strong ground motion prediction toward earthquake disaster mitigation," grant-in-aid for Science Research 14002116, and the research grant awarded by the Japan Society for the Promotion of Science (JSPS) under the "FY2002 JSPS Postdoctoral Fellowship for Foreign Researchers" from the Ministry of Education, Science, Sports and Culture of Japan. Finally, we express our sincere thanks to the Editor and the anonymous referees for constructive reviews and valuable suggestions.

References

Anders, M. H., and D. V. Wiltschko, Microfracturing, paleostress and the growth of faults, *J. Struct. Geol.*, *16*, 795–815, 1994.

Andrews, D. J., Rupture velocity of plane-strain shear cracks, *J. Geophys. Res.*, *81*, 5679–5687, 1976.

Atkinson, B. K., *Fracture Mechanics of Rock*, Academic, San Diego, Calif., 1987.

Broek, D., *The Practical Use of Fracture Mechanics*, Kluwer Acad., Norwell, Mass., 1989.

Brune, J. N., Tectonic stress and the spectra of seismic shear waves from earthquakes, *J. Geophys. Res.*, *75*, 4997–5009, 1970.

Cox, S. J. D., and C. H. Scholz, Rupture initiation in shear fracture of rocks: An experimental study, *J. Geophys. Res.*, *93*, 3307–3320, 1988.

Dalguer, L. A., Simulação de Movimentos Sísmicos Considerando o Mecanismo de Ruptura da Falha Causativa do Terremoto, Doctoral dissertation, Dep. of Civ. Eng., Fed. Univ. of Rio Grande do Sul, Porto Alegre R. S., Brazil, 2000.

Dalguer, L. A., K. Irikura, J. Riera, and H. C. Chiu, Fault dynamic rupture simulation of the hypocenter area of the thrust Fault of the 1999 Chi-Chi (Taiwan) earthquake, *Geophys. Res. Lett.*, *28*, 1327–1330, 2001a.

Dalguer, L. A., K. Irikura, J. Riera, and H. C. Chiu, The importance of the dynamic source effects on strong ground motion during the 1999 Chi-Chi, Taiwan, earthquake: Brief interpretation of the damage distribution on buildings, *Bull. Seismol. Soc. Am.*, *95*, 1112–1127, 2001b.

Dalguer, L. A., K. Irikura, W. Zhang, and J. Riera, Distribution of dynamic and static stress changes during 2000 Tottori (Japan) earthquake: Brief interpretation of the earthquake sequences; foreshocks, mainshock and aftershocks, *Geophys. Res. Lett.*, *29*(16), 1758, 10.1029/2001GL014333, 2002.

Day, S. M., Three-dimensional simulation of spontaneous rupture: The effect of nonuniform prestress, *Bull. Seismol. Soc. Am.*, *72*, 1881–1902, 1982.

Fukuyama, E., and R. Madariaga, Rupture dynamic of a planar fault in a 3D elastic medium: Rate- and slip-weakening friction, *Bull. Seismol. Soc. Am.*, *88*, 1–17, 1998.

Fusejima, Y., T. Yoshioka, K. Mizuno, M. Shishikura, R. Imura, T. Komatsubara, and T. Sasaki, Surface rupture associated with the 2000 Tottori-ken Seibu earthquake (in Japanese), in *Annual Report on Active Fault and Paleoearthquake Research*, no.1, Geol. Surv. of Jpn., Natl. Inst. of Adv. Ind. Sci. and Technol., Tsukuba, 2000.

Griffith, A. A., The phenomena of rupture and flow in solids, *Philos. Trans. R. Soc. London, Ser. A*, *221*, 163–198, 1920.

Harris, R. A., and S. M. Day, Dynamic 3D simulations of earthquakes on en echelon faults, *Geophys. Res. Lett.*, *26*, 2089–2092, 1999.

Ida, Y., Cohesive force across the tip of a longitudinal-shear crack and Griffith's specific surface energy, *J. Geophys. Res.*, *77*, 3796–3805, 1972.

Inoue, D., K. Miyakoshi, K. Ueta, and S. Abe, Geological survey of active faults around the 2000 Tottori-Seibu earthquake (in Japanese), *Nucl. Viewpoints*, *47*, 66–71, 2001.

Lajtai, E. Z., A theoretical and experimental evaluation of the Griffith theory of brittle fracture, *Tectonophysics*, *11*, 129–156, 1971.

Madariaga, R., Dynamics of an expanding circular fault, *Bull. Seismol. Soc. Am.*, *66*, 639–666, 1976.

Madariaga, R., K. Olsen, and R. Archuleta, Modeling dynamic rupture in a 3D earthquake fault model, *Bull. Seismol. Soc. Am.*, *88*, 1182–1197, 1998.

Moore, D. E., and D. A. Lockner, The role of microfracturing in shear-fracture propagation in granite, *J. Struct. Geol.*, *17*, 95–114, 1995.

Nayfeh, A. H., and M. S. Hefsy, Continuum modeling of three-dimensional truss-like space structures, *AIAA J.*, *16*, 779–787, 1978.

Ohnaka, M., Y. Kuwahara, and K. Yamamoto, Nucleation and propagation processes of stick-slip failure and normal stress dependence of the physical parameters of dynamic slip failure, *Nat. Disaster Sci.*, *9*, 1–21, 1987.

Olsen, K. B., R. Madariaga, and R. Archuleta, Three dimensional dynamic simulation of the 1992 Landers earthquake, *Science*, *278*, 834–838, 1997.

Petit, J. P., and M. Barquins, Can natural faults propagate under mode II conditions?, *Tectonics*, *7*, 1243–1256, 1988.

Reches, Z., and D. A. Lockner, Nucleation and growth of faults in brittle rocks, *J. Geophys. Res.*, *99*, 18,159–18,173, 1994.

Riera, J. D., and M. Rocha, A note on the velocity of crack propagation in tensile fracture, *Rev. Bras. Cienc. Mec., RBCM*, *XII*(3), 217–240, 1991.

Scholz, C. H., Mechanism of creep in brittle rock, *J. Geophys. Res.*, *73*, 3295–3302, 1968.

Scholz, C. H., *The Mechanics of Earthquakes and Faulting*, Cambridge Univ., New York, 1990.

Vermilye, J. M., and C. H. Scholz, The process zone: A microstructural view of fault growth, *J. Geophys. Res.*, *103*, 12,223–12,237, 1998.

Yamashita, T., Generation of microcracks by dynamic shear rupture and its effects on rupture growth and elastic wave radiation, *Geophys. J. Int.*, *143*, 395–406, 2000.

L. A. Dalguer and K. Irikura, Disaster Prevention Research Institute, Kyoto, Kyoto University, Gokasho, Uji, Kyoto 611-0011, Japan. (dalguer@egmdpri01.dpri.kyoto-u.ac.jp; irikura@egmdpri01.dpri.kyoto-u.ac.jp)

J. D. Riera, Curso de Pós Graduação de Engenharia Civil, Universidade Federal de Rio Grande do Sul, Av. Osvaldo Aranha 99, 3° andar, CEP, 90035-190, Porto Alegre, R.S. Brazil. (riera@genesis.cpgec.ufrgs.br)

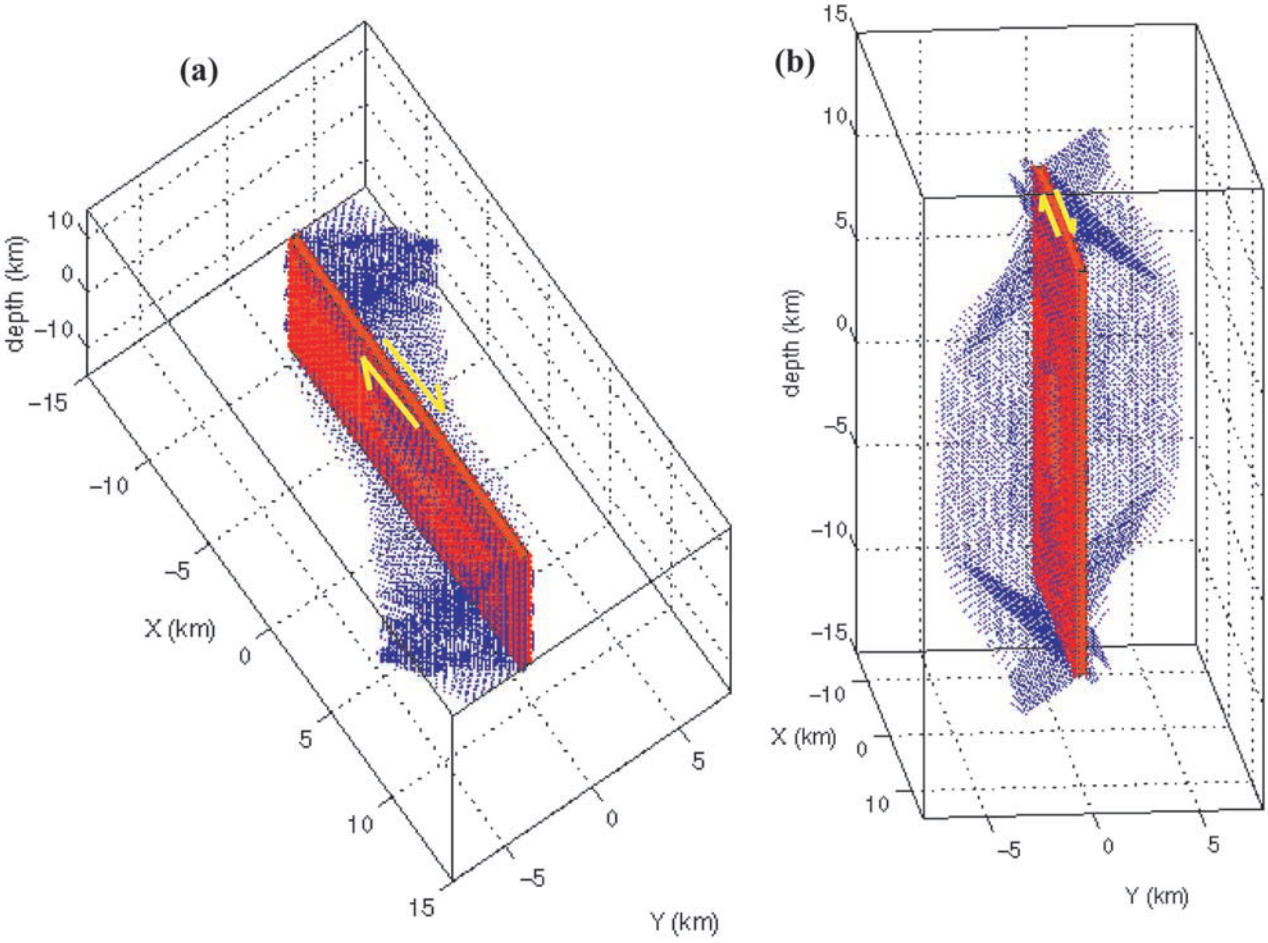

Figure 7. Two perspectives of the final stage of the crack evolution for a homogeneous fault model embedded in an unbounded medium with no free surface. Red denotes the shear crack on the preexisting fault, and blue denotes tensile cracks. (a) View of new surface cracks that grew from the sides of the fault and (b) view of new surface cracks forming flower-like structures that originated from the bottom and top boundaries of the fault.

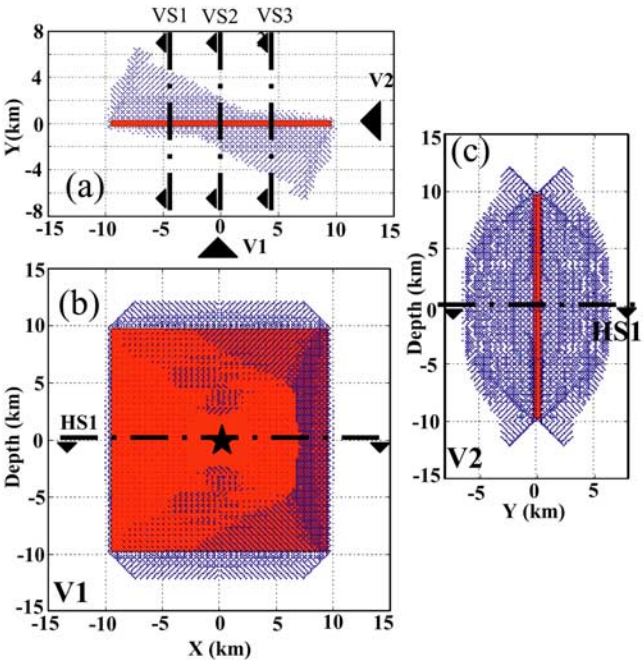

Figure 8. Views of the final stages of the crack evolution for a homogeneous fault model embedded in an unbounded medium with no free surface. (a) Bird's-eye view, (b) frontal view (V1), and (c) outline view (V2).

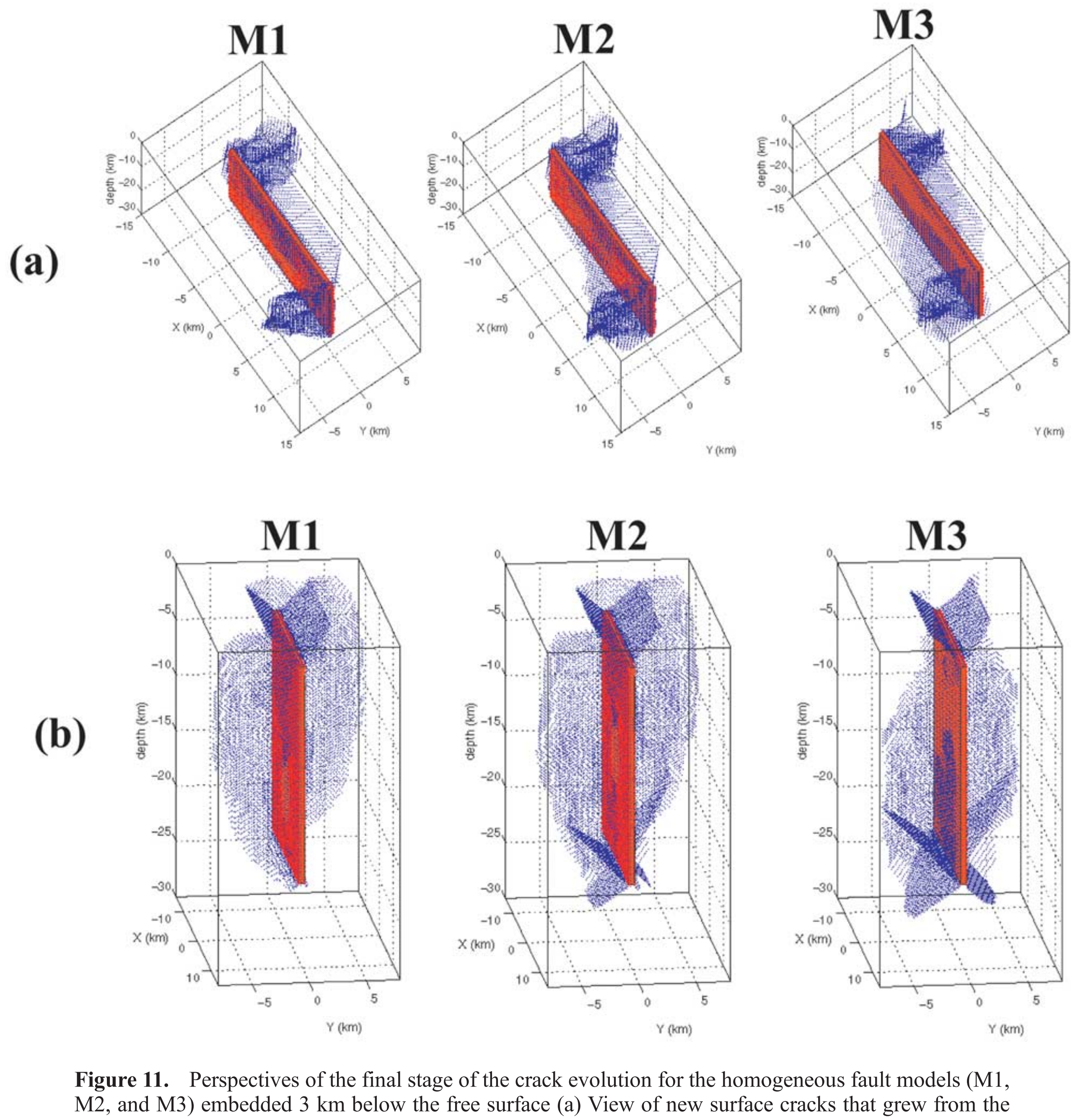

Figure 11. Perspectives of the final stage of the crack evolution for the homogeneous fault models (M1, M2, and M3) embedded 3 km below the free surface (a) View of new surface cracks that grew from the sides of the fault and (b) view of new surface cracks forming flower-like structures that originated from the bottom and top boundaries of the fault.

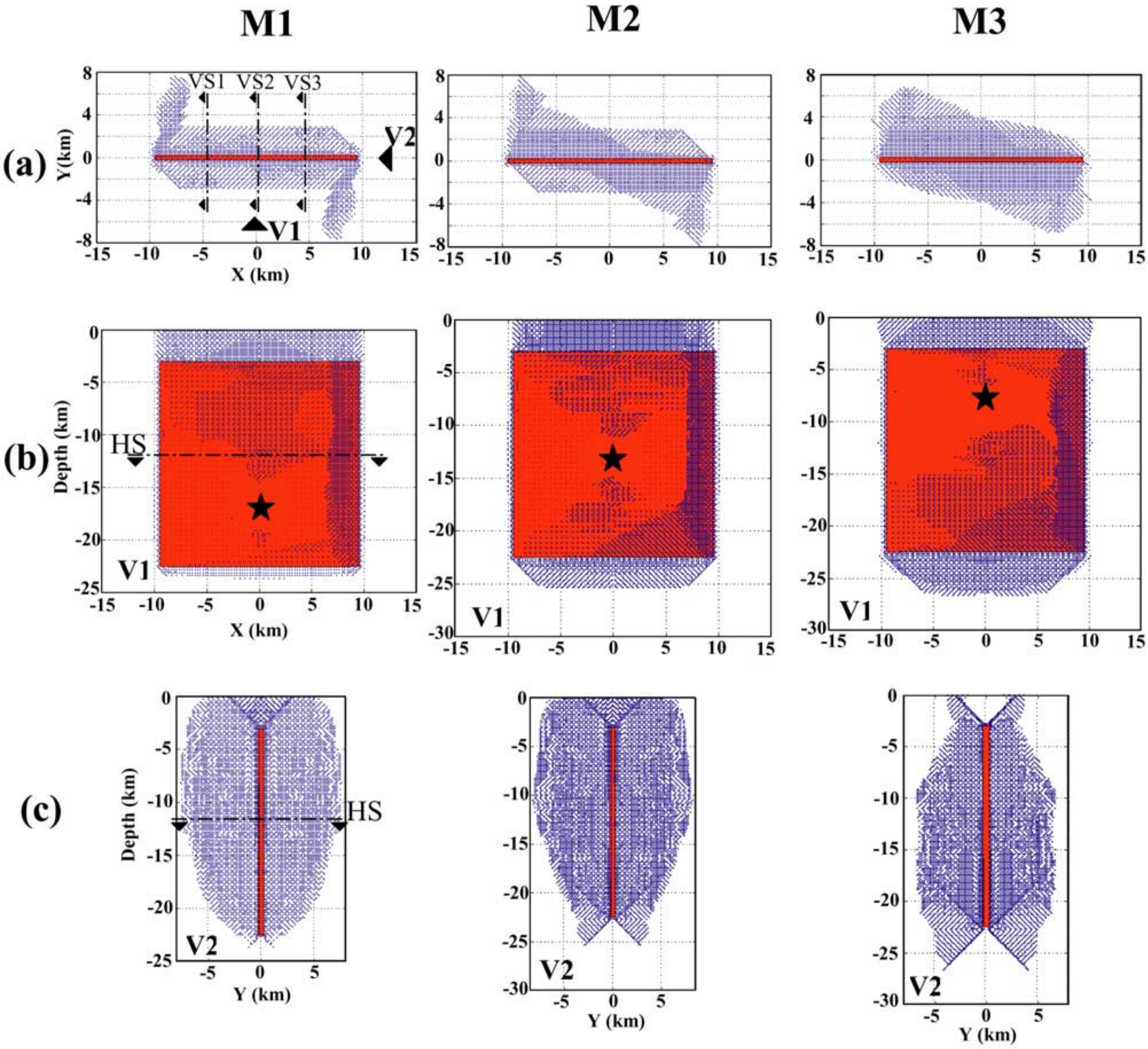

Figure 12. Views of the final stage of crack evolution for the homogeneous fault models (M1, M2, and M3) embedded 3 km below the free surface. (a) Bird's eye view, (b) frontal view (V1), and (c) outline view (V2).

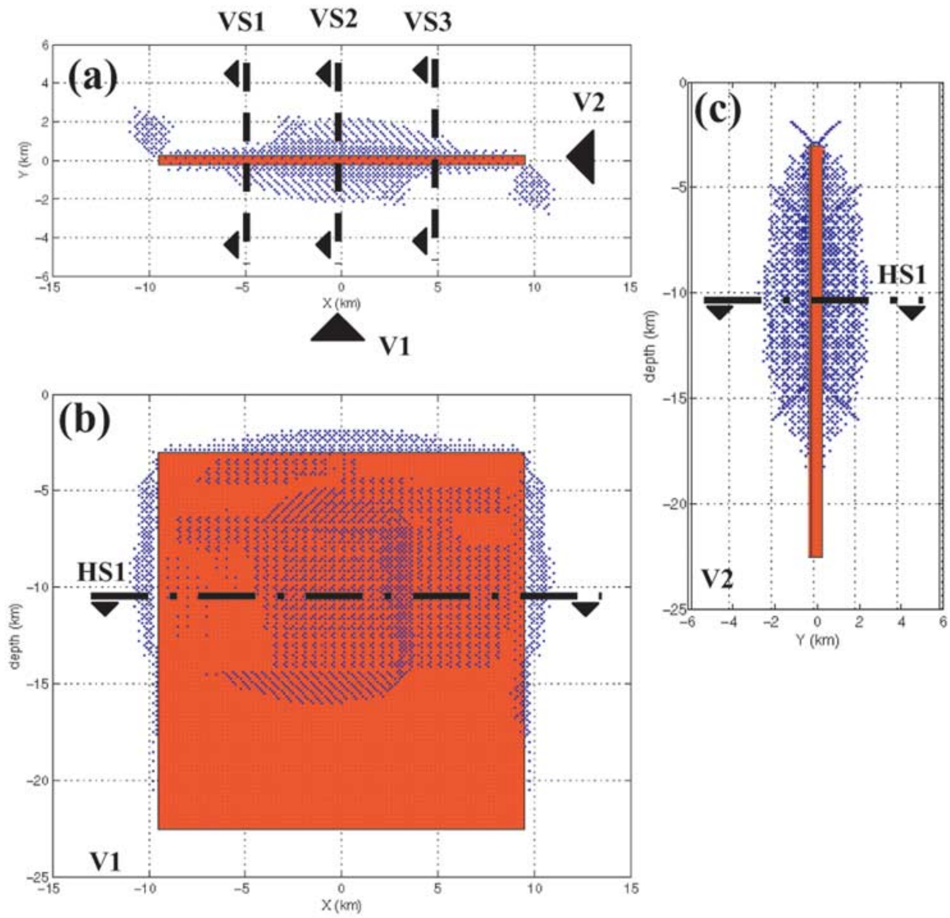

Figure 16. Views of the final stage of crack evolution for the asperity model (H = 4.0 km). (a) Bird's-eye view, (b) frontal view (V1), and (c) outline view (V2).

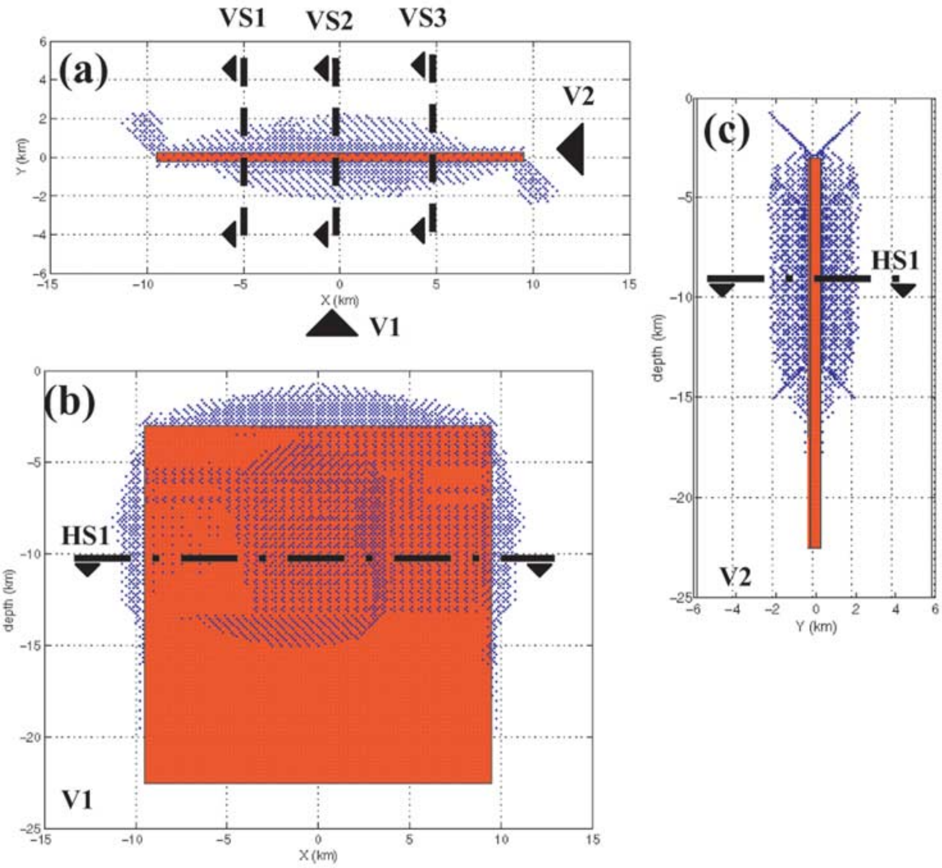

Figure 17. Views of the final stage of crack evolution for the asperity model (H = 3.0 km) (a) Bird's-eye view; (b) frontal view (V1); (c) outline view (V2).

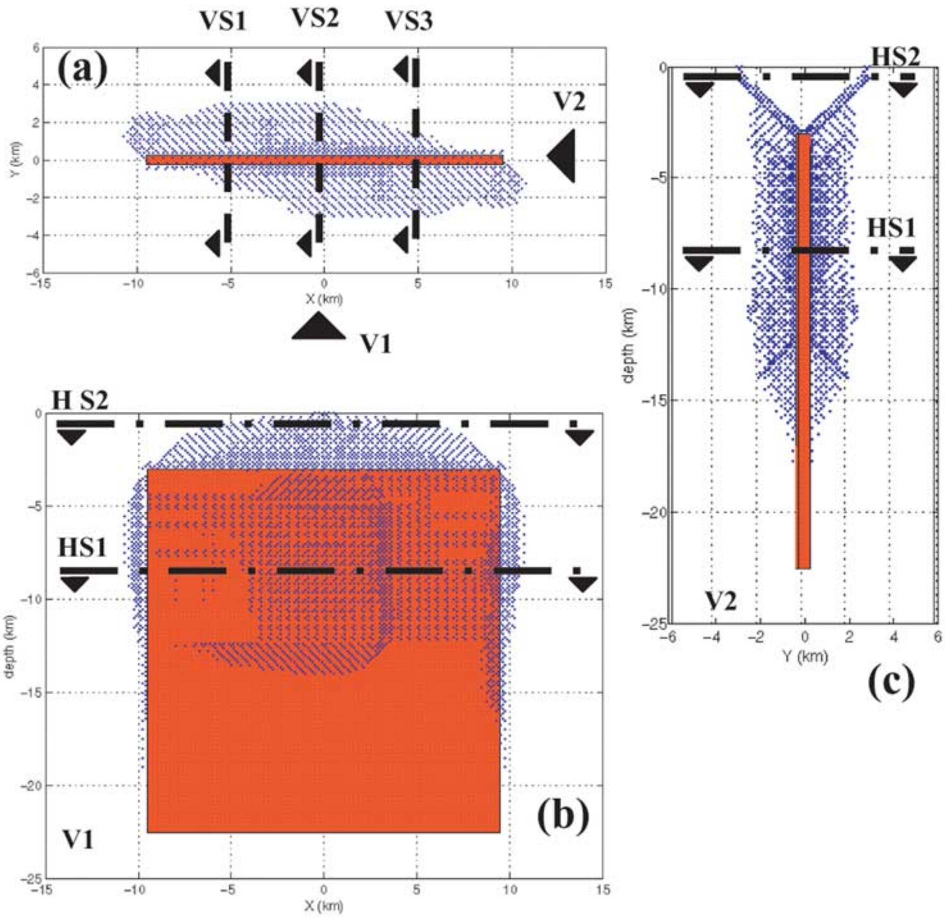

Figure 18. Views of the final stage of crack evolution for the asperity model (H = 2.0 km). (a) Bird's-eye view, (b) frontal view (V1), and (c) outline view (V2).

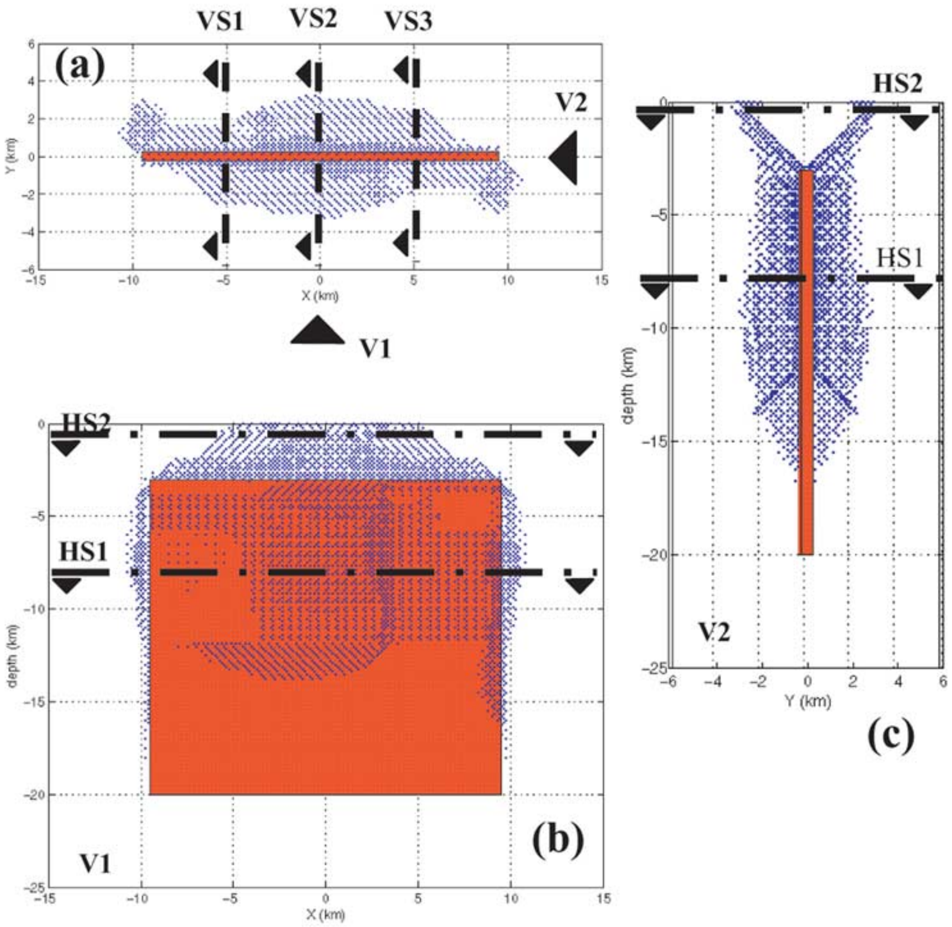

Figure 19. Views of the final stage of crack evolution for the asperity model (H = 1.5 km). (a) Bird's-eye view, (b) frontal view (V1), and (c) outline view (V2).

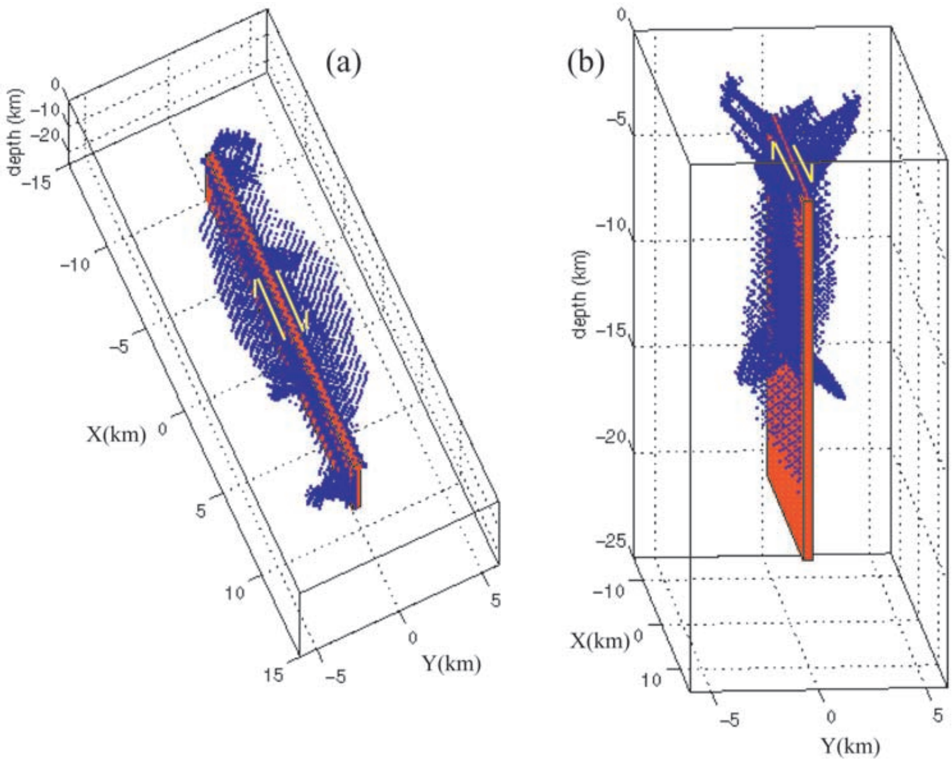

Figure 22. Two perspectives of the final stage of the crack evolution for an asperity fault model (H = 1.5 km). Red denotes the shear crack on the preexisting fault, and blue denotes tensile cracks. (a) View of new surface cracks that grew from the sides of the fault and (b) view of new surface cracks forming flower-like structures that originated from the bottom and top boundaries of the fault.